



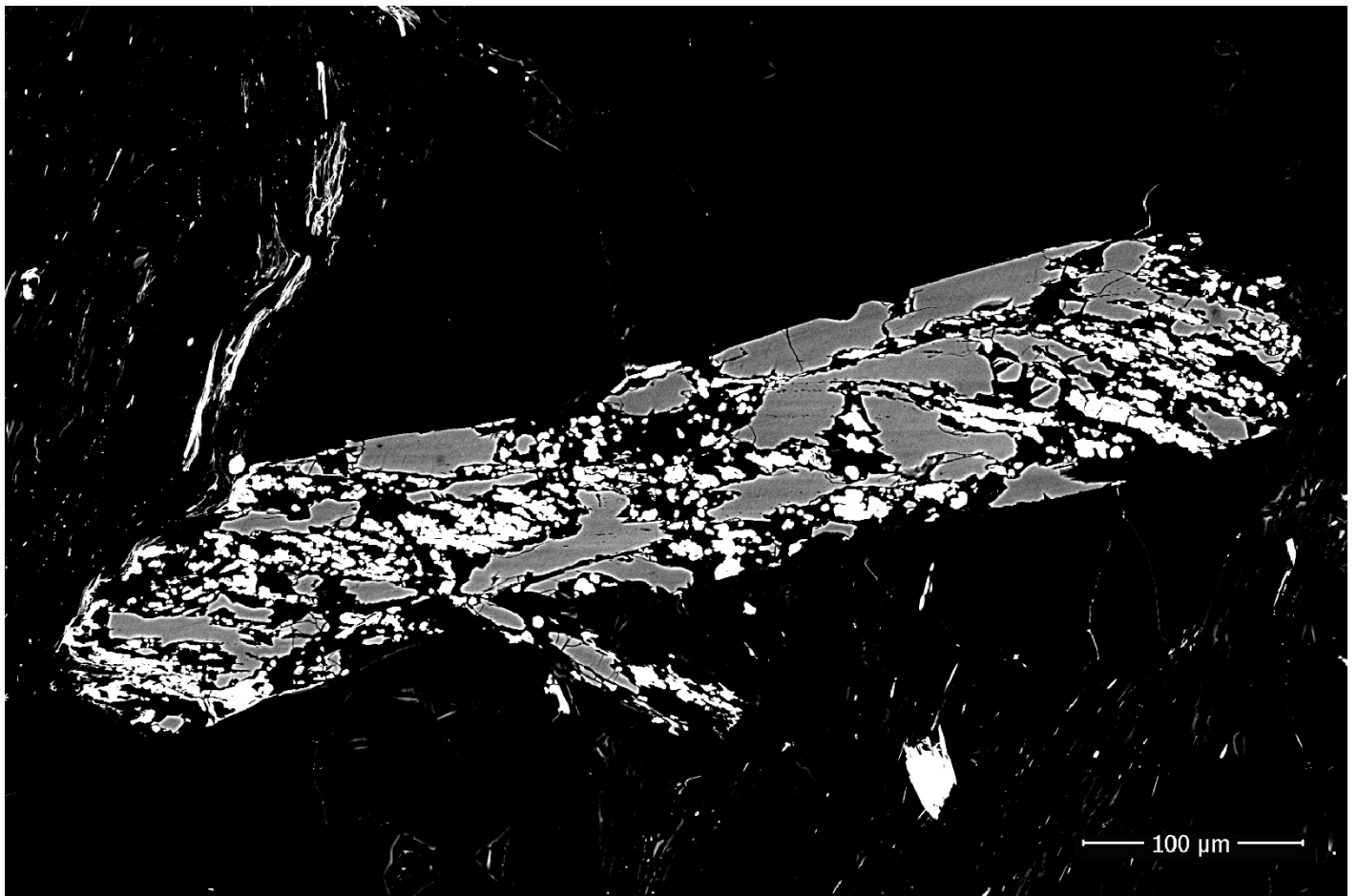
Stockholm
University

Master Thesis

Degree Project in
Geology 45 hp

Chloritoid occurrences in the Saih Hatat window (Oman): Stability and bulk-rock chemical control

Sandra Morawiecki



Stockholm 2023

Department of Geological Sciences
Stockholm University
SE-106 91 Stockholm

Chloritoid occurrences in the Saih Hatat window (Oman): Stability and bulk-rock chemical control

Abstract

The pressure and temperature conditions reached by metamorphic rocks are commonly inferred using silicates minerals. Most of them, such as chloritoid and sodic amphiboles, contains iron (Fe): this chemical element can be present as ferrous (Fe^{2+}) or ferric (Fe^{3+}) iron. In this respect, the oxidation state of a rock influences the stability field of Fe-bearing minerals. Therefore, it is crucial to evaluate the influence of the oxidation state of a rock on the stability field of the minerals used for geothermobarometry. This study explores the stability of chloritoid in metapelites from Oman (focusing on the Hulw Unit) investigating the bulk and chloritoid chemistry and comparing these results with literature data from other metamorphic terrains. The bulk rock compositions of chloritoid-bearing metapelites from this study and from the reviewed articles can be divided into three main groups based on their Al_2O_3 and Fe_2O_3 content. The results show that Mg-rich chloritoid is mainly found in rocks characterised by high Al_2O_3 content, whereas Fe^{2+} - and Fe^{3+} -rich chloritoid occurs in Al_2O_3 -poor and Fe_2O_3 -rich rocks. Metapelites containing Fe-oxides, such as hematite, display the highest bulk ferric iron ratio ($\text{Fe}^{3+}/\text{Fe}^*$). In some cases, hematite partially replaces chloritoid, suggesting that hematite is a late mineral, grown after chloritoid possibly as a result of oxidation. Overall, the ($\text{Fe}^{3+}/\text{Fe}^*$) is systematically higher in the bulk than in chloritoid. However, a high bulk $\text{Fe}^{3+}/\text{Fe}^*$ does not directly imply a high $\text{Fe}^{3+}/\text{Fe}^*$ in chloritoid. Instead, both the coexisting minerals as well as the Al_2O_3 and Fe_2O_3 contents in the bulk play an important role in the stability and chemistry of chloritoid. To properly evaluate the relationship between $\text{Fe}^{3+}/\text{Fe}^*$ in the bulk and in the rock-forming minerals, a focus on pristine chloritoid-bearing rocks, that have not been influenced by any later oxidation stage, would be considered.

Table of contents

1. INTRODUCTION	3
2. GEOLOGICAL SETTING	4
2.1 Architecture of the Al Hajar mountains	4
2.2 Metamorphic history of the SHD	5
3. THEORETICAL BACKGROUND	7
3.1 Chloritoid	7
4. METHODS	8
4.1 Petrography	8
4.2 Bulk-rock geochemistry	9
4.3 Mineral chemistry	10
5. RESULTS	12
5.1 Petrographic observations	12
5.2 Bulk rock chemistry	23
5.3 Chemical composition of chloritoids	28
5.3.1 Binary diagrams of chloritoid crystals in sample 11 and sample 13	29
5.3.2 Chloritoid chemistry (samples 11 and 13)	32
5.3.3 Chloritoid chemistry from literature review	33
6. DISCUSSION	42
6.1 Chloritoid occurrences in the Saih Hatat window (Oman)	42
6.1.1 Oxidation of Oman rocks	43
6.1.2 Chloritoid zonation in sample 11 and 13	44
6.2 Chloritoid occurrences in metapelites: bulk-rock chemical control	44
7. CONCLUSIONS	46
Acknowledgements	47
References	48

1. INTRODUCTION

Subducted rocks undergo metamorphism and change their mineralogy in a convergent setting according to a Franciscan facies series (high pressure, low temperature). A common index mineral for high pressure-low temperature (HP-LT) metapelites (> 7 kbar, $<600^{\circ}\text{C}$) is chloritoid. In metapelites, chloritoid is often found together with quartz + white mica + chlorite \pm accessory minerals, and this mineral is inferred to have formed under blueschist facies conditions. However, recently Manzotti et al., (2020) showed that in the case of sodic amphiboles, their stability is heavily influenced by the bulk composition and the oxidation state of the rock. The authors show that sodic amphiboles can, in some circumstances, form in upper greenschist facies conditions and are therefore a poor indicator for blueschist facies. Similarly, ferric iron affects the stability field of the major rock forming silicates (eg. chloritoid, carpholite, garnet) that are used to gain valuable thermobaric information (Lo Po and Braga, 2014).

This brings the question of how the bulk composition and the oxidation state of the rock influence the stability of chloritoids and if chloritoid can stabilise at greenschist facies conditions. The oxidation state of a rock is affected by bulk rock composition derived from the sedimentary environment \pm fluid interactions (Holland and Worley, 2000) The oxidation state of a rock or a mineral is estimated by determining their ferric iron content (Fe_2O_3).

By combining a petrographic and geochemical investigation of the chloritoid-bearing metapelites of Oman with a literature review of metapelites from other metamorphic terrains, the role of bulk rock chemical control on the occurrence of chloritoid in metapelites has been explored. This study has the potential to provide important insights into the understanding of chloritoid and its composition. In addition, this study will mainly focus on the Hulw Unit, structurally located below the worldwide known ophiolite. Most studies in Oman have mainly focused on the ophiolite so far, whereas the underlying chloritoid-bearing metapelites (i.e. the Hulw Unit) have been generally disregarded. Therefore, this study also represents an opportunity to explore an underinvestigated area.

2. GEOLOGICAL SETTING

2.1 Architecture of the Al Hajar mountains

The Al Hajar mountains in north-eastern Oman (Figure 2.1) are a typical example of obduction, where the oceanic crust has been pushed on top of continental crust. These rocks are often poorly exposed, but they exceptionally crop out at the Saih Hatat dome (SHD) in Oman (Hansman et al., 2021), exhibiting the large Sumail ophiolite. In this area, mountains do not reach above 2000 m and the general relief is <500 m (Hansman et al., 2021). The SHD consists of continental rocks with ages ranging from Late Proterozoic to Ordovician at the base and Upper Permian to Upper Cretaceous at the top (Goffé et al., 1988). The Arabian plate was affected by a folding event during the formation of Pangea in the Palaeozoic (Goffé et al., 1988) and the rocks found at the base of the Saih Hatat dome were deformed, but high-pressure metamorphism did not occur in Oman until the Cretaceous (El-Shazly and Liou, 1991). Two tectonic models have been proposed to explain the tectonic history of the area:

- 1) single-event model with subduction and obduction occurring simultaneously, forming eclogite- and blueschist-facies rocks as well as lawsonite and carpholite-bearing rocks (Yamato et al. 2007).
- 2) multi-stage model, where subduction occurred first, forming eclogite- and blueschist-facies rocks followed by obduction of the oceanic plate, causing tectonic burial and producing lawsonite and carpholite-bearing rocks (Ring et al., 2023).



Figure 2.1. The Al Hajar Mountains in NE Oman, around the area of Muscat (Lat: 23.614328 N, Long: 58.545284 E). Source: <https://en-gb.topographic-map.com/>

2.2 Metamorphic history of the SHD

Mountain belts that have previously undergone deep subduction commonly exhibit high-pressure, low-temperature (HP-LT) rocks, such as blueschist and eclogite facies rocks (Yamato et al., 2007). Some of the Oman HP rocks were subducted at depths greater than 80 km during Upper Cretaceous and were later exhumed in a contractional tectonic setting, with the latest stages of exhumation occurring after ~60 Ma by normal faulting (Hansman et al., 2021). The HP-LT metamorphic rocks located below the ophiolite are poorly studied and they were first described by Michard et al. (1981) and Bailey (1981).

The rocks at the base exhibit covers of metagreywacke and stromatolitic dolostone interlayered with conglomerates, quartz rich sandstones and siltstones (Goffé et al., 1988), which have been metamorphosed into blueschist and eclogite facies rocks, as well as lawsonite and carpholite bearing rocks (Hansman et al., 2021). The younger rocks constitute of conglomerates and shallow water carbonates (Goffé et al., 1988) with the Hawasina nappe and the Sumail ophiolite at the top (Ring et al., 2023). The metamorphic grade is increasing from top to bottom of the

sequence, with the Ruwi Unit being at the top of the metamorphosed rocks followed by the Wadi Mayh/Saih Hatat Unit. There is later a strong strain gradient called the Upper Plate-Lower Plate (UP-LP) discontinuity (Ring et al., 2023). Below the UP-LP discontinuity is the Hulw Unit and the As Sifah Unit, the highest-pressure Unit, at the base (Yamato et al., 2007). The Hulw unit and the As Sifah unit are separated by the As Sheik shear zone, which marks a big break in metamorphic grade (Ring et al., 2023).

The Ruwi Unit and the Wadi Mayh/Saih Hatat Unit records similar pressure (3-9 kbar) and temperature (180-350 °C) conditions (El-Shazly, 1994; Goffé et al., 1988; Agard et al., 2010) and display carpholite-bearing rocks (Yamato et al., 2007; Agard et al., 2010). The Hulw Unit, which is located under the UP-LP discontinuity, shares similar P-T history as the UP rocks and records P-T conditions of 7-9 kbar and 400-460 °C (Yamato et al., 2007), but with slightly higher-pressure peaks of 11-12 kbar (Yamato et al., 2007). In this Unit, chloritoid-bearing rocks have been described by Yamato et al., 2007; El-Shazly, 1995; El-Shazly and Liou, 1991). The As Sifah Unit is the highest-pressure unit with eclogite facies rocks that experienced P-T conditions of 10-16 kbar and temperatures up to 585°C (El-Shazly et al., 1990; Hansman et al., 2021). Temperature estimates were made on the Hulw Unit and As Sifah Unit by Yamato et al. (2007) by using RAMAN spectroscopy on carbonaceous material. The temperature ranges they received were between 363-585°C with an overall SSE trending temperature increase (Figure 2.2).

This study investigates a few samples collected in the Ruwi, Wadi Mayh/Saih Hatat and Hulw Units. Specifically, a detailed investigation has been conducted on chloritoid-bearing rocks from the Hulw Unit. The samples were collected by Andreas Scharf in 2021.

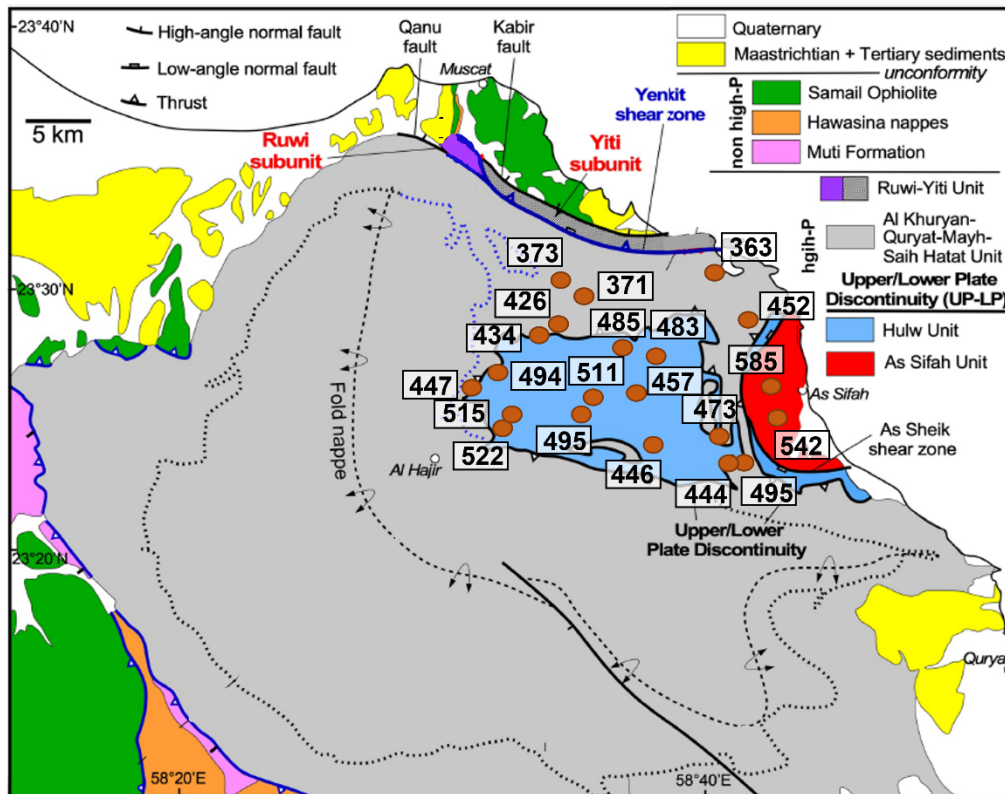


Figure 2.2. Map showing temperature measured with RAMAN (Yamato et al., 2007). Modified map with geology from Ring et al. (2023).

3. THEORETICAL BACKGROUND

3.1 Chloritoid

Chloritoid commonly occurs in Al-rich protoliths (MacKenzie et al., 2017) typically in phyllites, schists and marbles, and can be used as a zone mineral between chlorite and staurolite (Goffé et al., 1988). Traditionally, chloritoids are thought as a blueschist facies mineral, however, chloritoid can form in various conditions, depending on the bulk composition and assemblage of minerals in the rock. For instance, chloritoid is stable between 375-600°C but starts to transform to staurolite between 500-575°C (Ganguly, 1969) (Figure 3.1). Chloritoid has a solid-solution substitution between iron and magnesium end members and can incorporate Fe^{3+} and Ti^{4+} by substituting Al^{3+} . The ferric iron content in chloritoid increases with pressure, from <0.038 a.p.f.u. at 10 kbar to 0.20 a.p.f.u. at 30 kbar (Vidal et al., 1994). The authors predict

that blueschist facies chloritoid should contain ferric iron. In higher grade rocks, chloritoid is consumed to form garnet. During retrograde metamorphism (when temperatures decrease from 450-500°C to 350-400°C) garnets in metapelites can be replaced by chlorite + quartz ± chloritoid (Goffé et al., 1988). In the Hulw Unit, Goffé et al. (1988) described the replacement of chloritoid by a low-grade assemblage of kaolinite and iron oxides. More generally, the breakdown of chloritoid during retrogression is commonly associated with the formation of iron oxides (Ganguly and Newton, 1968).

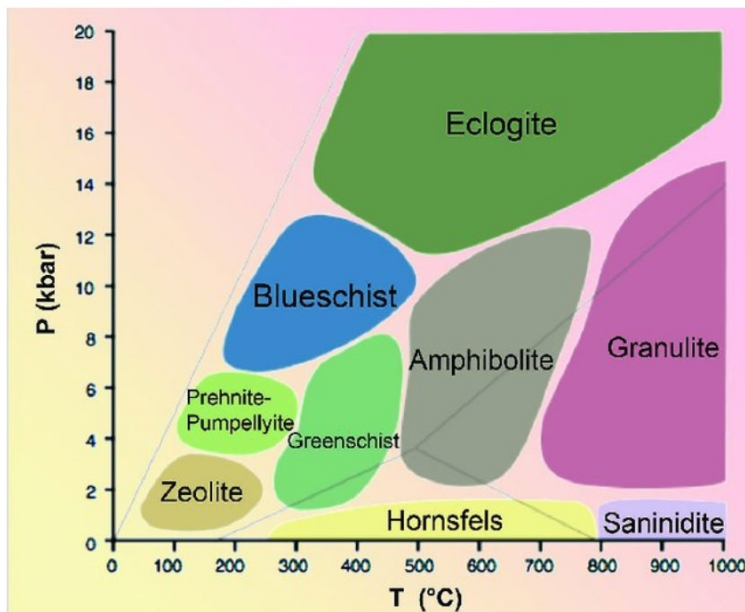


Figure 3.1. Summary of the metamorphic facies. Picture taken from Arndt (2013).

4. METHODS

4.1 Petrography

9 thin sections have been investigated in this study. Optical petrography was conducted on polished thin sections using a transmitted light microscope for mineral abundance estimation, textural relationships, and microstructural analysis. In addition to mineral observations and recognition, microscopy was also used to detect the textures of the minerals and how they

were organized in the thin section, i.e., if there was a foliation and/or if there were more than one stage of deformation. The mineral percentages were estimated visually.

The mineral abbreviations used in this study are listed below:

Ab-albite, Ank-ankerite, Car-carpholite, Cal-calcite, Cb-carbonate mineral, Chl-chlorite, Cld-chloritoid, Dol-dolomite, Ep-epidote, Fsp-Feldspar, Gr-graphite, Grt-garnet, Hem-hematite, Ms-muscovite, Prl-pyrophyllite, Pg-paragonite, Ph-phengite, Py-pyrite, Qz-quartz, Rt-rutile, Stp-Stilpnomelane, Tur-tourmaline, Wm-white mica. All mineral abbreviations are taken from Whitney and Evans (2010).

4.2 Bulk-rock geochemistry

XRF

The bulk rock composition of samples 11 and 13 from the Hulw Unit were measured. The samples were crushed and milled at Stockholm University. The samples were first crushed with a geological hammer and later milled in a Resch PM400 tungsten steel mortar with a speed of 800 rpm (rounds per minute) for 40+ seconds (Table 4.1). Between each sample milling the instruments and all the surfaces used during the process were cleaned thoroughly with ethanol to remove any possible contamination. After the samples were milled into a fine silt, they were transferred into plastic containers. 5 mg of each sample were moved into glass jars and sent to SARM-CRPG Nancy (France)

Major elements were determined by ICP-AES (SARM-CRPG, Nancy). Bulk-rock glasses were fused at 980 °C by mixing appropriate proportions (1 %) of fine-grained rock powder with di-lithium tetraborate. Then, glasses were dissolved in a mixture of HNO₃ (5%), H₂O₂ (0.5%) and glycerol (10%) prior to analysis. Details about the method used for the analyses are available in Carignan *et al.* (2001). Uncertainties at 1σ are *c.* 5% for the ICP-AES data. In addition, separate analyses of Fe²⁺ content of whole-rock samples were performed (SARM-CRPG, Nancy, France) by titration with potassium dichromate after dissolution of the sample in a HF/H₂SO₄ mixture, in the presence of H₃BO₃ and H₃PO₄.

Table 4.1 Sample 11 and 13 were milled twice per batch. One batch was the amount that fit into the milling device. R1= round 1. R2= round 2.

Sample n	11 (R1)	11 (R2)	13 (R1)	13 (R2)
Batch 1	40s	15s	40s	20s
Batch 2	40s	20s	40s	25s
Batch 3	40s	0s	40s	20s

The bulk rock compositions are given in wt.% (Appendix, Table 1) Molecular proportions have been calculated for plotting the data in AFM diagram.

In this study, the following symbols are used for the bulk rock compositions:

1. Fe_2O_3^* = Total iron of a bulk expressed as Fe_2O_3 (wt.%)
2. Bulk $\text{Fe}^{3+}/\text{Fe}^*$ = $\text{Fe}^{3+}/\text{Fe}^{2+}\text{Fe}^{3+}$ (calculated using the molecular proportions)
3. Mg# = $\text{MgO}/(\text{MgO}+\text{FeO})$ (calculated using the molecular proportions)
4. $\text{Fe}^{3+}/\text{Fe}^*$ = $\text{Fe}^{3+}/\text{Fe}^{2+}\text{Fe}^{3+}$ (for chloritoid, calculated using the a.p.f.u.)

4.3 Mineral chemistry

SEM

Further analyses were done for chloritoid, oxides and carbonates on samples 11a, 11b and 13, using a scanning electron microscope (SEM, FEI Quanta 650 FEG) at the Natural History Museum in Stockholm. The sample preparation consisted of carbon coating on polished thin sections to avoid charging of electrons. The current used for imaging was 20.00 kV. with contrast: ~52.29 and brightness: ~94,148 for large scale images and contrast: ~60.59 and brightness: ~88.038 for detailed images.

Scanning electron microscopy (SEM) is applied to gain high spatial resolution imaging of minerals. The SEM uses electrons for scanning the minerals, providing qualitative chemical compositional data as mean atomic numbers. Electron scanning is conducted in a vacuum to remove scattering and achieve images with a magnification of up to 500 000x. The images show higher atomic weights as brighter contrasts on a black and white scale. Depending on the detection mode, compositional or topographic contrasts can be acquired (Reed, 2005). The brightness is proportional to the atomic weight of the mineral/ion, where brighter means greater

atomic weight. The program Aztec is used for spot analysis to determine which elements are present in the mineral (eg K, Na etc).

EMPA

Chloritoid analyses were performed with a Cameca SX100 electron microprobe (Microsonde Ouest, Brest, France) operating in the wavelength dispersive mode. Operating conditions for spot analyses were set to 15 keV, 20 nA and 10 s counting time on the peak (spot size = 1 μm). The $\phi(\rho Z)$ matrix correction was applied based on Pouchou & Pichoir (1985). Standards were natural albite (Na, Si), orthoclase (K), corundum (Al), wollastonite (Ca), forsterite (Mg), MnTiO₃ (Mn, Ti), andradite (Fe).

Chloritoid analyses have been performed by Jessica Langlade, the lab manager of the Microprobe laboratory of the Ifremer (Brest, France), but I have chosen the position of the spot under the guidance of my MSc supervisor.

Microprobe data from the samples from this study, and a summary of the main characters of chloritoid for the reviewed samples is found in appendix (Table 2 and 3, respectively).

AX

AX is a freeware activity-composition program for rock-forming minerals. The program recalculates the analysis to a mineral formula. The assumptions used in deriving the activities and in estimation of ferric iron for chloritoid are listed below.

- **Chloritoid**

Ferric from: Cation Sum = 4 for 6 oxygens. $R_{\text{max}} = 0.2$

For the half formula size used, there is one M2 site (Fe, Mg, Mn) and half a M1 site (Al, Fe³⁺) and so: $a_{\text{mctd}} = X_{\text{Mg,M2}} X_{\text{Al,M1}}^{0.5} \gamma_{\text{mctd}}$

Nonideality is approximated by renormalising to the set of endmembers mctd-fctd-mnctd with symmetric formalism interaction energies (kJ)

W	fctd	mnctd
mctd	1.5	1.5
fctd		1.5

The cations are based on the stoichiometric formula of chloritoid; $(\text{Fe, Mg, Mn}) \text{Al}_2\text{SiO}_5(\text{OH})_2$ with the sum of 4 cations for 6 oxygen. The database used for estimation of ferric iron are found in Holland and Powell, 1990 and 1998.

5. RESULTS

5.1 Petrographic observations

In the following, a detailed petrographic description of the samples is presented. The map of Figure 5.1 shows the location of the investigated samples. GSP coordinates of the samples are reported in Table 5.1, followed by detailed thin section descriptions, starting with sample 1A, and finishing with sample 15.

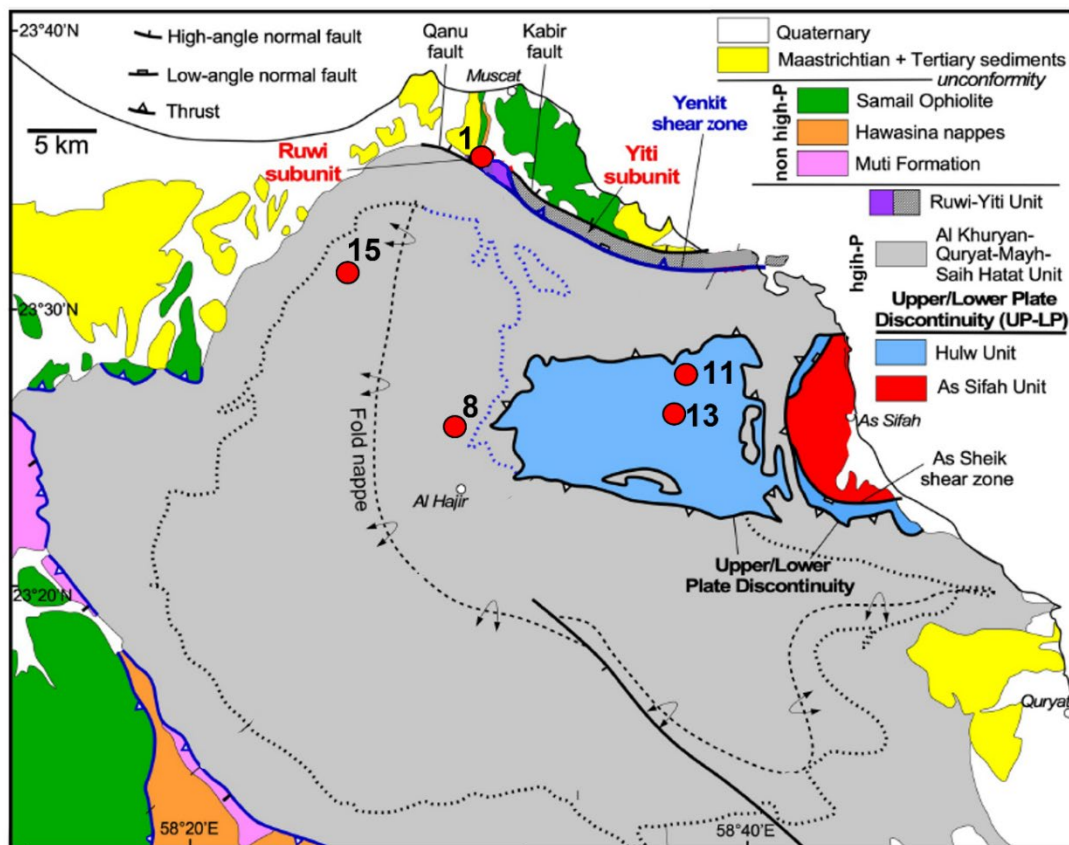


Figure 5.1. A map of NE Oman showcasing the locations of the studied samples. Modified map with geology from Ring et al. (2023).

Table 5.1. GPS coordinates for the collected samples

Sample name	Thin section name	Lithological type	GSP coordinates
1	1A	Phyllite/Carbonate	23°35'40.9" N 58°32'27.8" E
8	8A 8B	Phyllite	23°25'01.8" N 58°31'40.2" E
11	11A 11B 11C 11D	Mica schist	23°27'41.9" N 58°40'15.9" E
13	13	Mica schist	23°25'47.6" N 58°39'56.4" E
15	15	Mica schist	23°30'51.8" N 58°27'34.6" E

Ruwi Unit

Sample 1A

Sample 1A is a phyllite collected in the Ruwi Unit. The thin section has two different domains (figure 5.2a). One part is very fine grained with a matrix consisting of quartz and sericite. The other part of the thin section is coarse-grained and dominated by carbonates. The fine-grained part has thin schistosity surrounding porphyroclasts of quartz, carbonates and amphibole pseudomorphs (figure 5.2b) and small mica fisheye lenses (figure 5.2c). Their (001) planes are at a high angle to the rock cleavage (subparallel to the foliation). The small mica fisheye lenses show lower birefringence colours than the matrix sericite. The quartz porphyroclasts contain small rutile crystals, which are also found in the matrix of the rock. The sericite is growing into the porphyroclasts, breaking them apart. The deformation is mostly top to the left. The mica lenses are also deformed in uneven patterns and show both top to the left and top to the right deformation adjacent to each other. The other half of the thin section has slightly bigger grain size, with calcite/dolomite as the main constituent and up to 5% opaques. Some of the carbonates are square/diamond shaped which would indicate dolomite. Further to the right corner, the carbonates are anhedral and have more defined twinning with clear colours typical for calcite crystals. These carbonates could be identified as calcite. The carbonate rich part of the thin section contains almost no mica but has the same fisheye lenses, just as in the fine-

grained part. These are more oxidized and with a brown colour both in plane-polarised light (PPL) and crossed-polarised light (XPL) (figure 5.2d), leading to the interpretation of it being either oxidized mica or biotite/stilpnomelane. This part of the thin section has more tourmalines. There are two generations of tourmalines, where the older ones have foliation. There have later been overgrown with non-foliated tourmalines. The foliated ones are blue in PPL and the non-foliated ones are green/yellow. The oxidation in this thin section is concentrated in veins, growing on the carbonate. The rock has small crenulations in the matrix, but the direction of deformation is not visible. The contact between the two lithologies shows mostly top to the left deformation, however. Tourmaline and rutile are most frequent in the contact. Mineral percentage estimations are reported in Tables 5.2a and 5.2b.

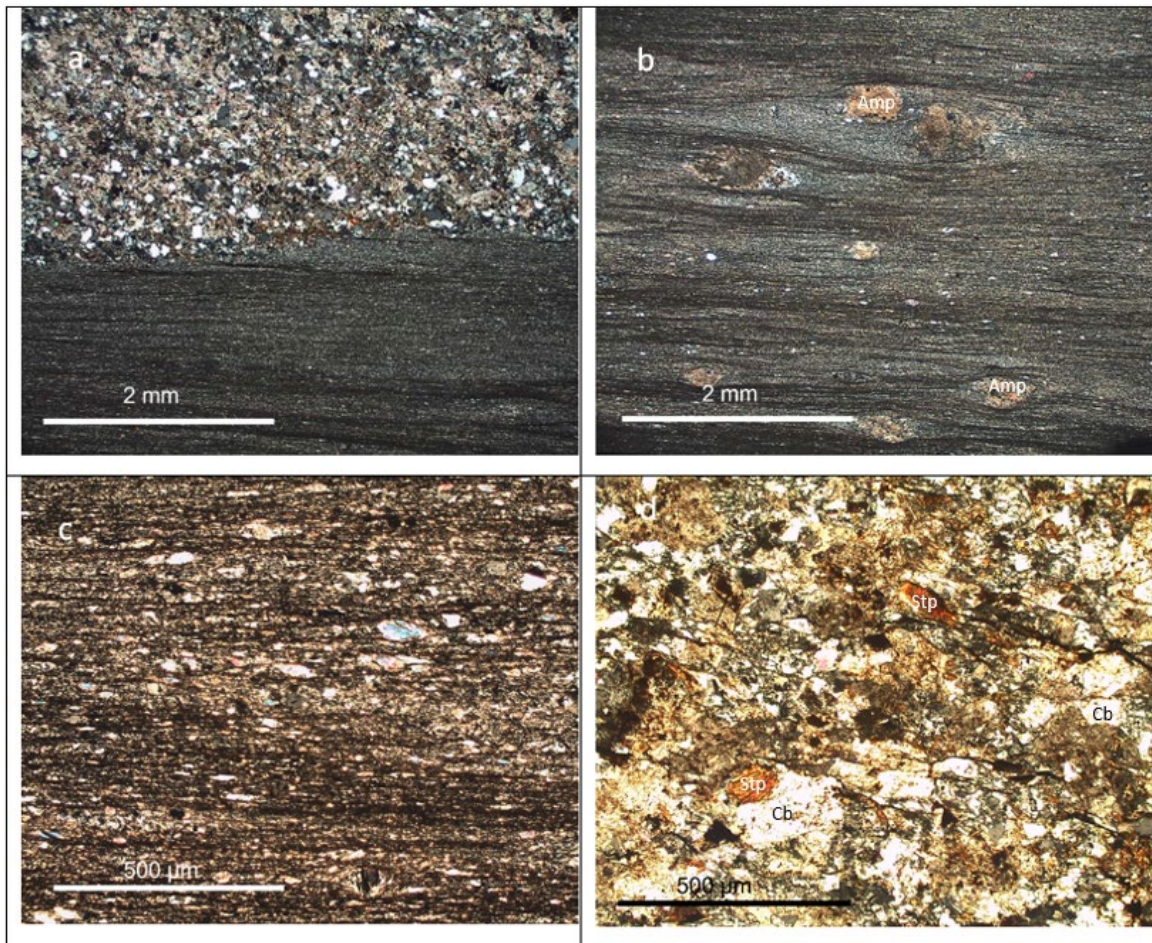


Figure 5.2. Thin section 1A. a) two different lithologies in the same sample. b) altered amphibole porphyroclasts in a fine-grained quartz-sericite matrix. c) fisheye lenses of mica in the fine-grained matrix. d) fisheye lenses of altered mica or stilpnomelane in the carbonate rich part of the thin section. The photos are taken with Leica microscope with 2.5x/10x objective. All photographs are taken XPL.

Table 5.2a. Mineral composition and distribution in the carbonate rich part of thin section 1A.

Mineral	Vol %	Stage 1 foliation	Stage 2 (retrograde)
Quartz	25	—————	
Dolomite	70	—————	
Stilpnomelane	2-3	
Oxide	2-3	
Rutile	<1	
Tourmaline	<1	

Table 5.2b. Mineral composition and distribution in the sericite rich part of thin section 1A.

Mineral	Vol %	Stage 1 foliation	Stage 2 (retrograde)
Quartz	55	—————	
White mica	35	—————	—————
Dolomite	5	—————	
Amphibole	5	—————	
Tourmaline	<1	
Rutile	<1	

Wadi Mayh Unit

Sample 8 (thin sections 8A and 8B)

Sample 8 is a phyllite collected in SW Wadi Mayh. The rock contains mostly quartz and mica and exhibits spaced schistosity (Figure 5.3a-b) with crenulations in the mica layers. The quartz is broken down and is penetrated by the mica (Figure 5.3c). The mica is deformed in an uneven pattern and could indicate different stages of growth. The rock is also rich in graphite (Figure 5.3d) and contains a minor part of tourmaline (yellow and green), epidote, rutile and magnetite (opaque mineral). The two thin sections 8a and 8b are very similar, but 8b contains more coarse-

grained quartz, which makes the rock seem to be less deformed. Mineral percentage estimations are reported in Tables 5.3a and 5.3b.

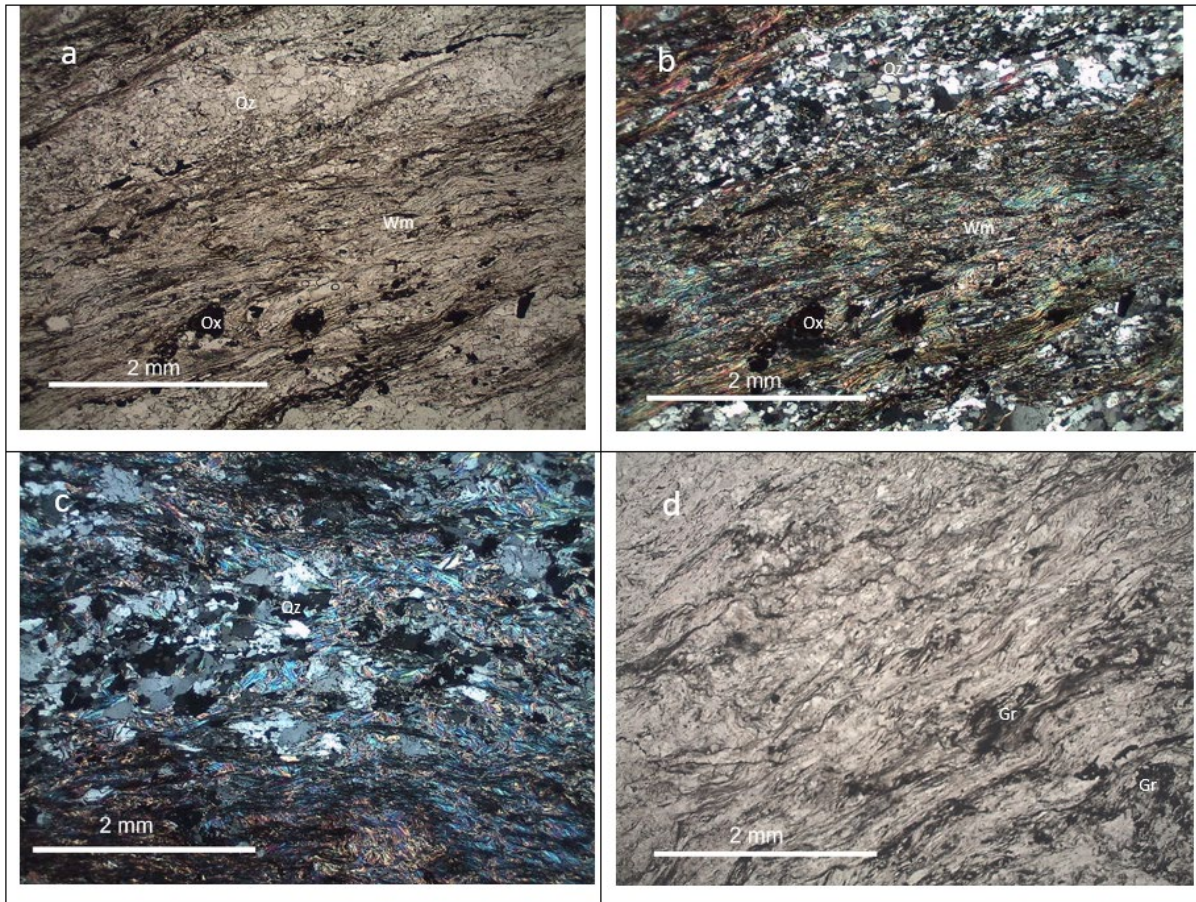


Figure 5.3. Photographs from thin section 8a and 8b. 3a. Spaced schistosity in ppl. 3b. Spaced schistosity in xpl. 3c. Mica penetrating older quartz crystals, shown in xpl. 3d. Graphite bands in ppl. The photos are taken with Leica microscope with 2.5x objective.

Table 5.3a. Mineral composition and distribution in thin section 8a. The accessory minerals are rutile, hematite, tourmaline and epidote.



















Mineral	Vol %	Stage 1 foliation	Stage 2 (retrograde)
Quartz	35		
White Mica	45		
Graphite	10		
Albite	5		
Accessory minerals	<5		

Table 5.3b. Mineral composition and distribution in thin section 8b. The accessory minerals are rutile, hematite, tourmaline, and epidote.

Mineral	Vol%	Stage 1 foliation	Stage 2 (retrograde)
Quartz	45		
White Mica	35		
Graphite	15		
Accessory minerals	<5		

Hulw Unit

Sample 11 (thin sections 11A, 11B, 11C, 11D)

Sample 11 is a mica schist from the Hulw unit. It is a quartz rich rock with clear mica and chlorite foliation (Figure 5.4a). The foliation is not crenulated, as in sample 8. Oxidized carbonates are concentrated in bands and are interpreted as ankerite. The ankerite is associated with chlorite (Figure 5.4b). Chloritoid crystals are found in all four thin sections and follow the foliation. Most chloritoid crystals are very small (~100-200 μm) but a few grains are up to 800 μm (Figure 5.4c). They are broken and partially altered by iron oxides and have quartz inclusions as well (Figure 5.4d). White mica is growing around the chloritoid (Figure 5.4d-e). The chloritoid is easily confused with tourmaline in this sample, as they have similar ocean blue colours in plane polarized light, although the tourmaline has reversed pleochroism (Figure 5.4e) whereas the chloritoid does not. The chloritoid also has inclusions of oxides, as mentioned before, and shows twinning in cross polars. The four thin sections show no significant differences and have similar volume percentages of the mineralogy. Mineral percentage estimations are reported in Table 5.4.

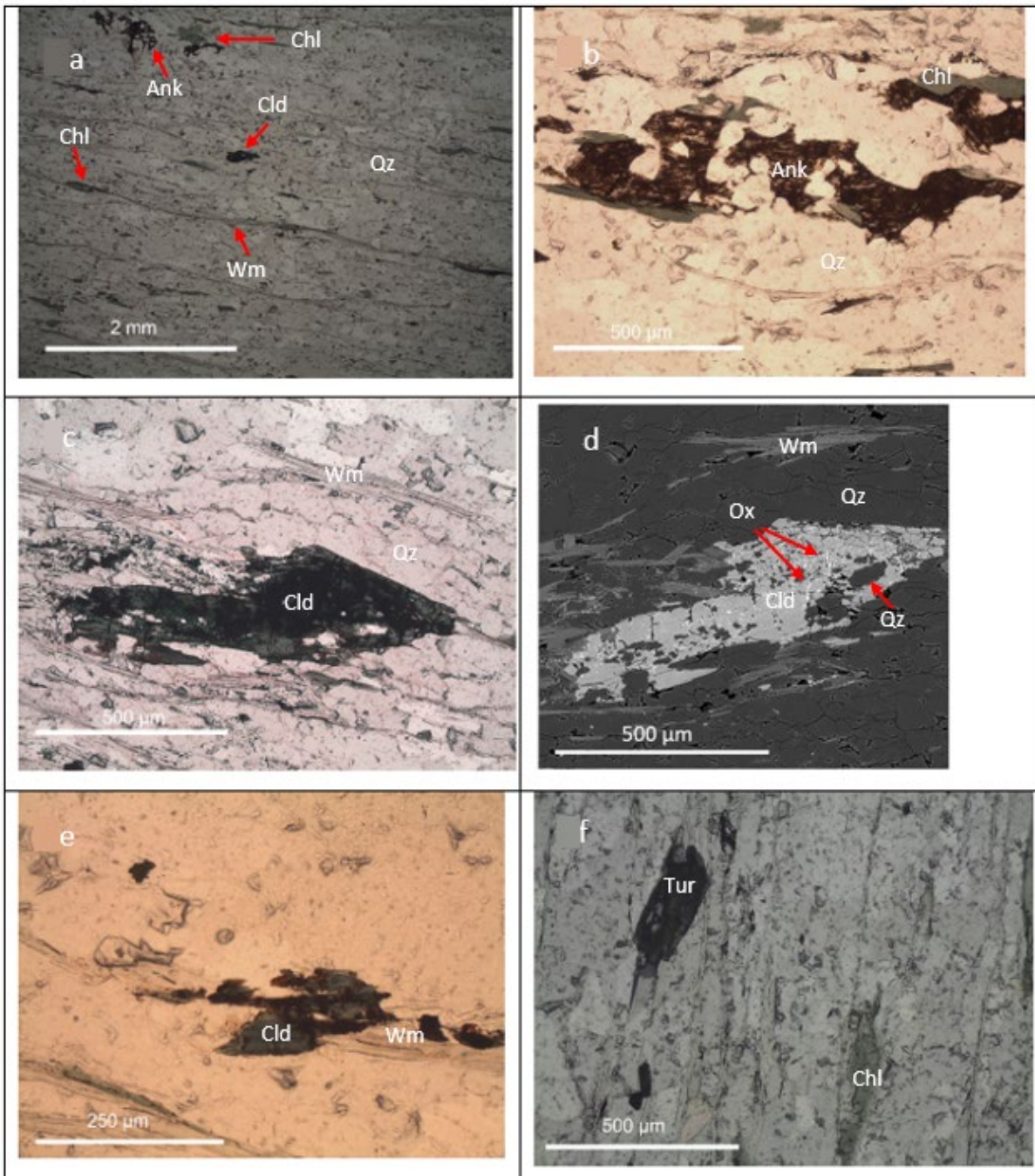


Figure 5.4. Photographs taken of thin section 11a-d. a) The foliation of the rock. b) Ankerite retrograded by chlorite. c) Chloritoid crystal with quartz inclusions, overgrown with iron oxides. d) SEM image of the chloritoid crystal shown in image c. e) White mica growing close to chloritoid. f) Tourmaline with reversed pleochroism (left) and chlorite (right). The photos are taken with Leica microscope with 2.5x, 10x and 20x objective in plane polarized light.

Table 5.4. Mineral composition and distribution in thin section 11a-d. The accessory minerals are chloritoid, rutile/goethite and tourmaline.

Mineral	Vol %	Stage 1 (foliation)	Stage 2 (retrograde)
Quartz	75	—————	—————
White Mica	10	—————	—————
Chlorite	5	—————	
Ankerite	8	—————	
Chloritoid	<1	
Oxides/accessory	<1	

Sample 13

Sample 13 is a mica schist from the Hulw unit. It displays a foliation marked by quartz layers; the shape preferred orientation of white mica mainly concentrated in film. Thin layers of oxides and hydroxides mainly consisting of hematite and goethite are oriented parallel to the main foliation. The mica to quartz ratio is higher in this rock compared to sample 11. In this sample, chloritoid is also more abundant than in sample 11, but chlorite has not been observed. The chloritoids are elongated (Figure 5.5a) and up to 700 μm long. They have a very weak blue/green colour in PPL with no pleochroism and 1st order colours and twinning in XPL, although it is hard to see the colours as the chloritoid is retrograded and replaced by oxides (Figure 5.5b). The oxides are dispersed in the matrix of the rock as well and are shaped as small round grains. The chloritoid crystals are mostly parallel to the foliation and follow the crenulation pattern, but a few crystals are almost perpendicular to the foliation (Figure 5.5c). The chloritoids are most concentrated around two bands of oxides (Figure 5.5d), one on the bottom of the thin section and one at the top. Figure 5.5e-f are SEM images showing the iron oxide bands in greater detail and the alteration of the oxides inside the chloritoid crystal. Hematite and goethite show concentric growth in some of the thin section (Figure 5.5 f). Mineral percentage estimations are reported in Table 5.5.

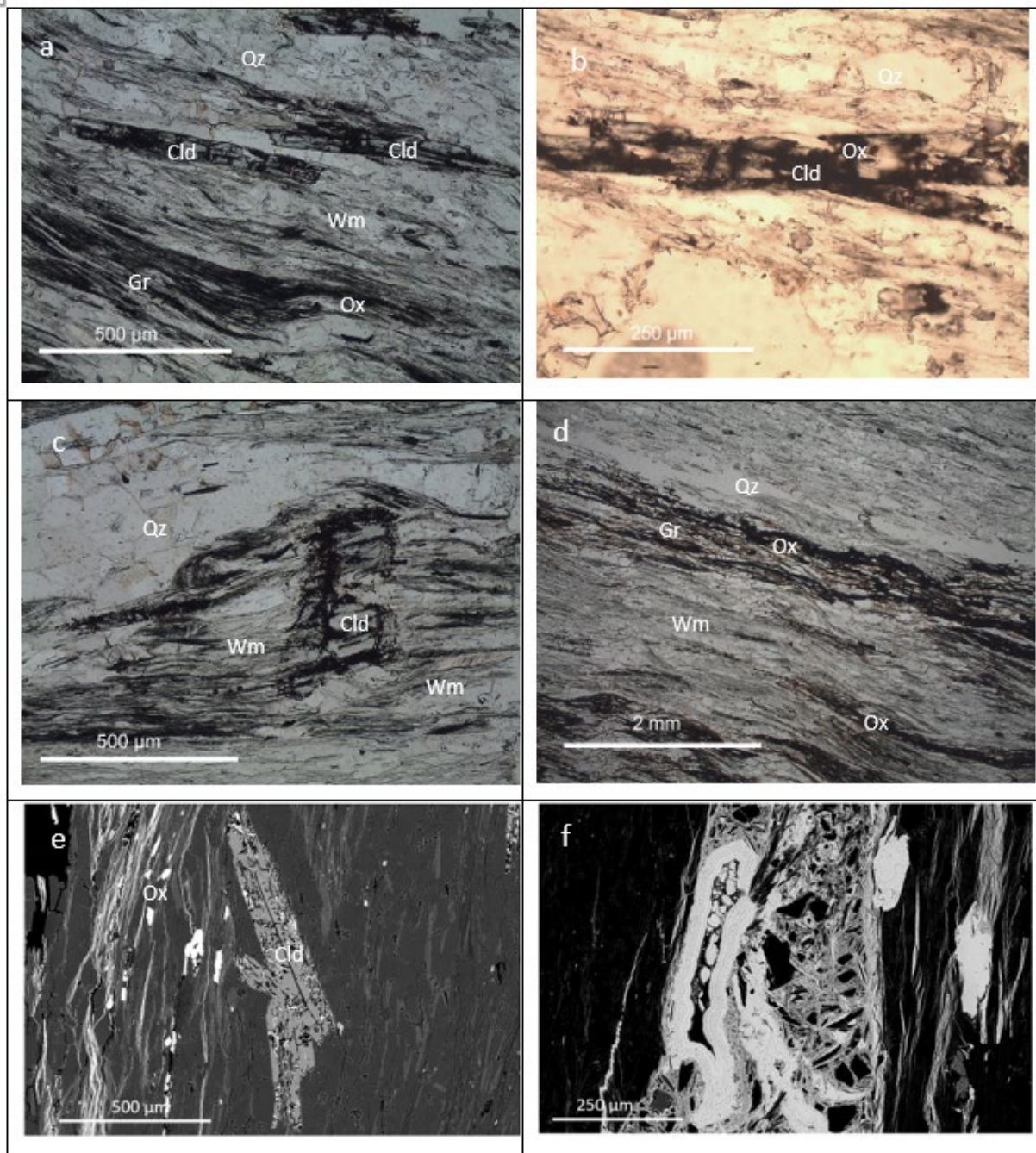


Figure 5.5. Petrographic photographs of thin section 13. a) Elongated chloritoid crystals. b) Oxidized and altered chloritoid crystal. c) Vertical chloritoid crystal, perpendicular to foliation. d) Chloritoid concentrated close to the oxidized bands in the thin section. e) SEM image of oxide bands (left side) and a chloritoid crystal altered by iron oxides (hematite). f) Iron oxides (hematite) and hydroxides (goethite). The photos are taken with Leica microscope with 2.5x, 10x and 20x objective in plane polarized light.

Table 5.5. Mineral composition and distribution in thin section 13.

Mineral	Vol%	Stage 1 foliation	Stage 2 (retrograde)
Quartz	25		
Mica	20		
Oxides & Hydroxides	20		
Chloritoid	10		
Graphite	10		
Rutile	<5		-----

Saih Hatat unit

Sample 15

Sample 15 is a mica schist from the Saih Hatat unit. It is crenulated and folded (Figure 5.6a-b). The mineralogy consists of primarily quartz and white mica with minor portions of feldspars and oxides, possibly also graphite. It also contains retrograded crystals of a carbonate mineral. The matrix consists of sericite with very fine-grained quartz with alternating bands of white mica and quartz. Most of the oxides are associated with the quartz. Sample 15 is similar to sample 13 in texture but is much more folded. Retrograded carbonates and feldspars crosscut the foliation or grow on top of other minerals in the foliation. Mineral percentage estimations are reported in Table 5.6.

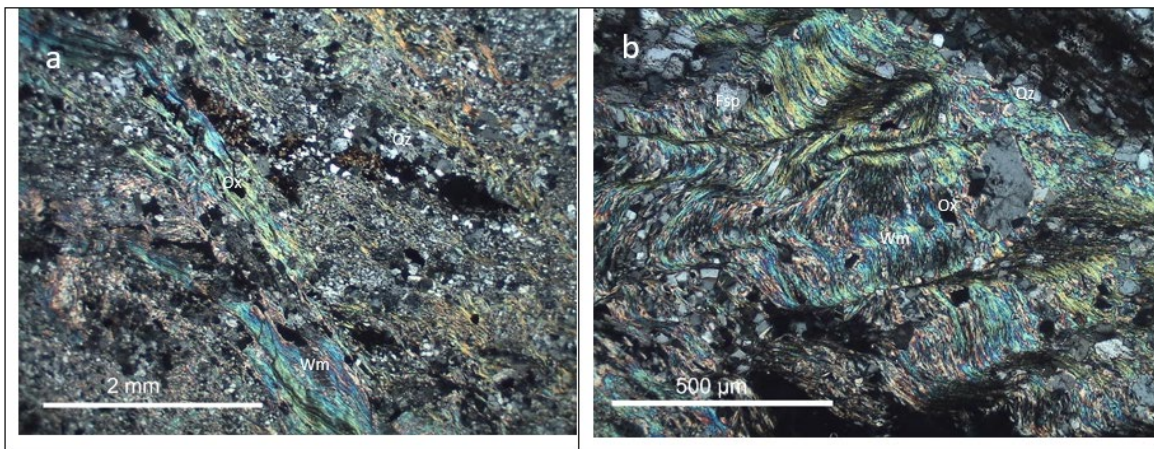


Figure 5.6. Petrographic photographs of thin section 15. a) a big fold going through the whole thin section. b) Crenulations/folds in the mica layers. The photos are taken with Leica microscope with 2.5x/10x objective in XPL.

Table 5.6. Mineral composition and distribution in thin section 15.

Mineral	Vol%	Stage 1 foliation	Stage 2 (retrograde)
Quartz	42	—————	
Mica	40	—————	—————
Feldspar	15	—————	
Oxides	2-3		—————
Carbonates	<1	

5.2 Bulk rock chemistry

This paragraph presents a literature review compiling bulk rock composition from chloritoid-bearing metapelites from different metamorphic terrains worldwide (Figure 5.7). Overall, according to the read studies, the geothermal gradient registered for the plotted rocks is comprised between 8 and 14 °C/km.



Figure 5.7. A map showing the metamorphic terrains considered in the literature review. From West to East: Betic Cordilleras (yellow), the Alps (grey), Apennines (black), the Calabride complex (pink), Crete (blue), Anatolia (green) and Saih Hatat (red). The samples investigated in this study have also been collected in Saih Hatat, Oman. Stars indicate terrains for which literature studies provide both bulk rock composition and chloritoid chemistry, whereas circles indicate terrains for which literature studies report only chloritoid chemistry.

The bulk rock compositions are plotted in an AFM [(Al₂O₃-3K₂O)-FeO-MgO] diagram projected from quartz, muscovite, and H₂O (Figure 5.8). This diagram aims (i) to evaluate how the bulk rock compositions of chloritoid-bearing metapelites vary and (ii) to correlate chemical variations to the P-T conditions experienced by the studied rocks. The main information on the samples taken from the literature are reported in Table 5.7.

Sample 11 and **13** from this study are plotted as red stars (Figure 5.8). Sample 13 is rich in Al₂O₃ (14.42 wt.%) whereas sample 11 is poor in Al₂O₃ (2.63 wt.%). Both samples are poor in Na₂O and K₂O (Sample 11: Na₂O = 0.02 wt.% K₂O = 0.74 wt.%, Sample 13: Na₂O = 1.41 wt.% K₂O = 2.02 wt.%).

Based on their Al₂O₃ content, the bulk rock compositions taken from the literature can be grouped into three different groups, namely Group 1, Group 2, and Group 3. Samples belonging to Group 1 display the highest Al₂O₃ content (19.96-31.13wt%), whereas samples of Group 3 are poor in Al₂O₃ (11.60 and 13.39 wt.%). Most of the samples plot in Group 2 and are characterised by Al₂O₃ in the range 9.88-29.14 wt.%.

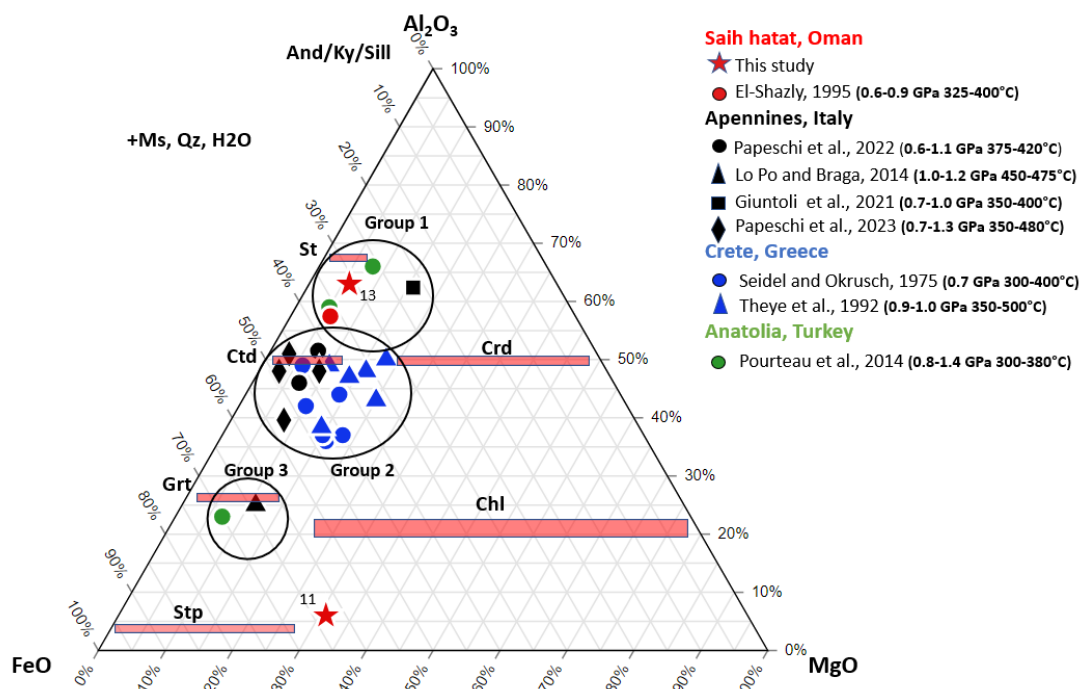


Figure 5.8. AFM [(Al₂O₃-3K₂O)-FeO-MgO] diagram projected from quartz, muscovite, and H₂O showing the bulk rock compositions of metapelites taken from the literature together with two key samples from this study (sample 11 and sample 13, plotted as red stars).

Compared to the bulk rock compositions of the chloritoid-bearing metapelites taken from the literature, the bulk composition of sample 13 is similar to the ones of Group 1, whereas sample 11 is very poor in Al_2O_3 (2.63 wt.%) and its composition is not comparable with the ones of the identified three groups. According to the temperature estimated for the plotted bulk rock composition taken from the literature, there may be a potential correlation between the T experienced by the samples and the Al_2O_3 content. Specifically, Al_2O_3 -rich rocks experienced lower temperature conditions (300-400°C) than Al_2O_3 -poor rocks (up to 500°C). By contrast, there is no correlation between the P experienced by the samples and their bulk composition (e.g. Al_2O_3 content): rocks characterised by different Al_2O_3 content records similar P conditions. However, these qualitative observations require further detailed investigations.

Table 5.7. Literature data compilation for the samples plotted in the ternary diagrams (Figures 2,3 and 4).

Mountain belt	Lithological unit	Rock type	Sample name	Mineral assemblage	P-T	Reference
Sah Hatat, Oman	Wadi Mijias	metapelite	Mj-10	car-qz-prl-ms-cld (<30%)	0.6-0.95 GPa 325-440°C	El-Shazly, 1995
Apennines	Monte Romani	cld-schist	R6	qz (50-60%) ms (20-30%) cld (5-10%) hem (1-5%) rt-pg (<1%)	0.6-1.1 GPa 375-420°C	Papeschi et al., 2022
Apennines	Monte Romani	cld-schist	R17	qz (50-60%) ms (20-30%) cld (5-10%) hem (1-5%) rt (<1%)	0.6-1.1 GPa 375-420°C	Papeschi et al., 2022
Apennines	Monte Prisanì	phyllite	MP4	qz (37%) ms (37%) chl (15%) hem (7%) cld (3%)	1.0-1.2 GPa 450-475 °C	Lo Po and Braga, 2014
Apennines	Monticiano-Roccalstrada	metapelite	Metapelite	ms (51%) qz (31%) pg (7%) prl (6%) cld (4%) rt (1%)	0.7-1 GPa 350-400°C	Giuntoli et al., 2021
Apennines	Massa	metapelite	SP308b	cld-ms-qz-gth-gr-tt-pg	0.7-1.3 GPa 350-480°C	Papeschi et al., 2023
Apennines	Massa	metapelite	SP332	cld-chl-ms-qz-hem-rt	0.7-1.3 GPa 350-480°C	Papeschi et al., 2023
Apennines	Massa	metapelite	SP329	cld-ms-pg-qz-hem-rt	0.7-1.3 GPa 350-480°C	Papeschi et al., 2023
Apennines	Massa	metapelite	SP319	ky-cld-ms-pg-prl-qz-hem-rt	0.7-1.3 GPa 350-480°C	Papeschi et al., 2023
Crete, Greece	Vouliklana	metapelite	72/68	qz-ms-cld (>20%) chl (<1%)	0.7 GPa 300-400°C	Seidel and Okrtsch., 1975
Crete, Greece	Vouliklana	metapelite	72/70	qz-ms-cld (>20%) chl (1-20%) cal-tur-prl (<1%)	0.7 GPa 300-400°C	Seidel and Okrtsch., 1975
Crete, Greece	Vouliklana	metapelite	73/163	qz-ms-cld (>20%) chl (<1%)	0.7 GPa 300-400°C	Seidel and Okrtsch., 1975
Crete, Greece	Anisaraki	metapelite	72/56	qz-ms-cld (>20%) cal (<1%)	0.7 GPa 300-400°C	Seidel and Okrtsch., 1975
Crete, Greece	Skafi	metapelite	72/96	qz-ms-cld (>20%) chl (<1%)	0.7 GPa 300-400°C	Seidel and Okrtsch., 1975
Crete, Greece	Asoires	metapelite	73/171	qz-ms-cld (>20%) chl (1-20%) cal (<1%)	0.7 GPa 300-400°C	Seidel and Okrtsch., 1975
Crete, Greece	Central Crete	metapelite	K84/314	qz-cld (>20%) chl-pg-ph-hem (2-20%) cal (<2%)	0.9 GPa 350°C	Theye et al., 1992
Crete, Greece	Central Crete	metapelite	K79/4	qz-cld-ph (>20%) cal-prl-pg-hem (2-20%)	0.9 GPa 350°C	Theye et al., 1992
Crete, Greece	Central Crete	metapelite	K79/8	qz-cld-car-ph (>20%) chl-hem (<2%)	0.9 GPa 350°C	Theye et al., 1992
Crete, Greece	Central Crete	metapelite	K74/203	cld-car-chl-ph (>20%) qz (2-20%) pg-hem (<2%)	0.9 GPa 350°C	Theye et al., 1992
Crete, Greece	Western Crete	metapelite	K76/107	qz-cld-chl-ph (>20%) pg-hem (<2%)	1.0 GPa 500°C	Theye et al., 1992
Crete, Greece	Western Crete	metapelite	K84/383	qz-cld-chl-ph (>20%) pg (2-20%)	1.0 GPa 500°C	Theye et al., 1992
Anatolia, Turkey	Afyon	phyllite	Af5P2	qz (>20%) car-cld-ph-prl (2-20%)	0.8-1.4 GPa 300-380°C	Pourteau et al., 2014
Anatolia, Turkey	Afyon	phyllite	Af5P3	qz (>20%) cld-ph (2-20%)	0.8-1.4 GPa 300-380°C	Pourteau et al., 2014
Anatolia, Turkey	Afyon	phyllite	Af5BP	car-ph-prl (>20%) cld (2-20%) chl-donb* (<2%)	0.8-1.4 GPa 300-380°C	Pourteau et al., 2014

The following ternary diagram (FeO-MgO-Fe₂O₃; Figure 5.9) is used to evaluate the content of FeO vs. Fe₂O₃ and its influence on the presence and composition of chloritoid. Sample 11 and 13 are plotted together with the available bulk rock compositions found in the literature. Unfortunately, not all studies have reported FeO and Fe₂O₃ content, but they simply indicated the total FeO content, generally expressed as Fe₂O₃ (i.e. Fe₂O₃*). For this reason, the bulk rock compositions of Group 1 are not plotted in Figure 3. Instead, we divide Group 2 from the AFM diagram (Figure 5.8) into two groups, namely Group 2a and 2b. Sample 11 plots in Group 2b and sample 13 in Group 3.

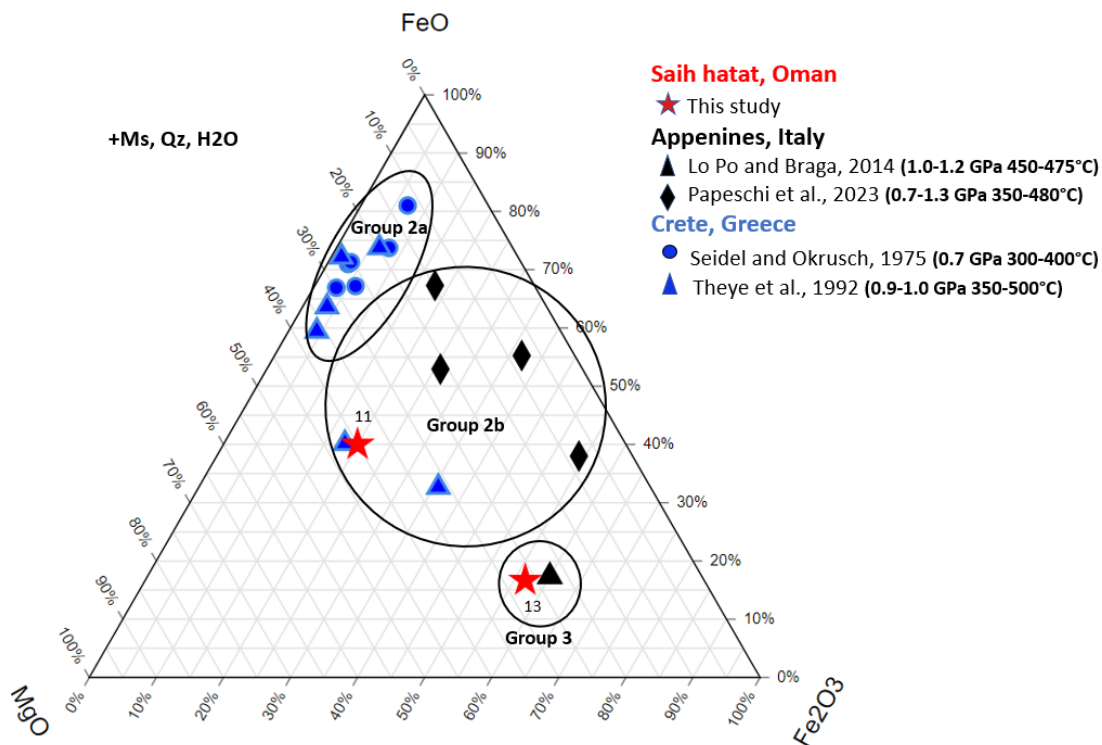


Figure 5.9. Ternary diagram plotting the MgO-FeO-Fe₂O₃ bulk rock compositions of metapelites from this study (stars) and from the literature. The plotted values are in molecular proportions recalculated on an anhydrous basis.

The Fe₂O₃, MgO and total iron (Fe₂O₃^{*}) is reported in Appendix, Table 3. Sample 11 displays a higher Fe³⁺/Fe^{*} ratio (0.77) than sample 13 (0.34). Its Fe³⁺/Fe^{*} ratio is comparable with the one displayed by one sample investigated by Lo Po and Braga (2014), equilibrated at 1.0-1.2 GPa and 450-475 °C. Samples 11 and 13 displays relatively low Mg# (0.50 and 0.62, respectively).

The AFF [(Al₂O₃-3K₂O)-FeO-Fe₂O₃] diagram of Figure 5.10 is projected from quartz, muscovite, and H₂O. The Fe₂O₃ content increase from group 2a to 2b, whereas group 3 is very spread out between its two samples. Sample MP4 from Lo Po and Braga (2014) is proportionally

highest in Fe₂O₃. Sample 11 is very poor in Al₂O₃, as seen in Figure 5.8, and is not added into group 2b for this diagram.

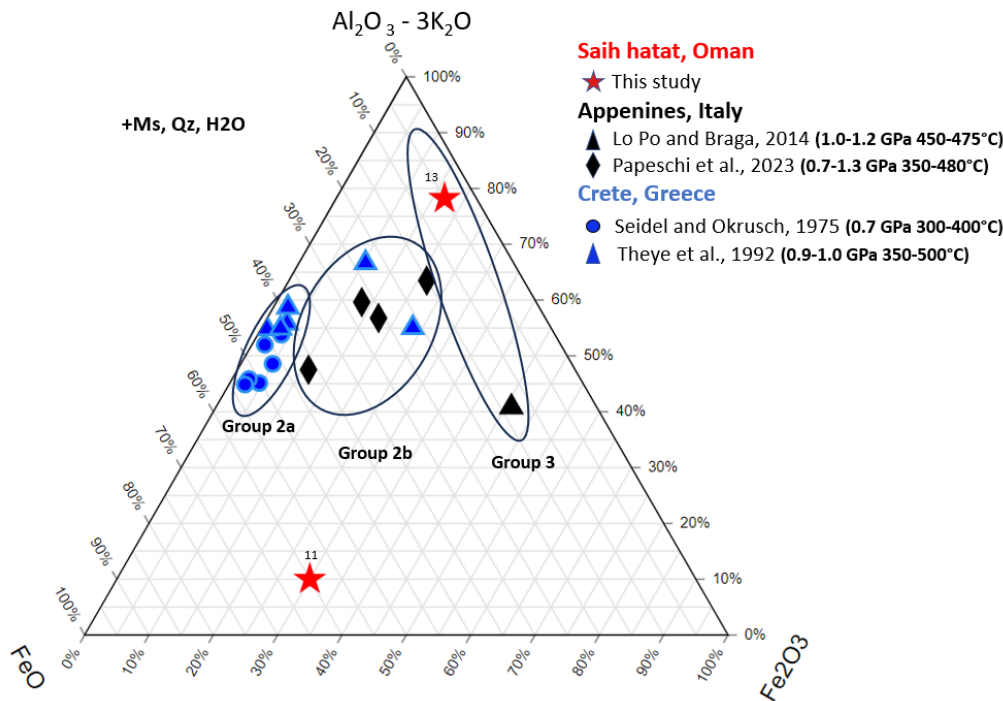


Figure 5.10. AFM [(Al₂O₃-3K₂O)-FeO-Fe₂O₃] diagram projected from quartz, muscovite, and H₂O showing the bulk rock compositions of chloritoid-bearing metapelites from this study (sample 11 and sample 13, plotted as red stars) and from the literature.

5.3 Chemical composition of chloritoids

This paragraph focuses on the texture and the chemical composition of chloritoid, with particular attention to the presence of Fe²⁺ vs Fe³⁺. Binary and ternary diagrams are used to highlight the chemical composition and internal zoning of chloritoid. The chemical composition of chloritoid from samples 11 and 13 investigated in this study will be first described in detail. Then, following the same approach used for the bulk rock chemistry, the chemical composition of chloritoid from this study will be compared with the ones of chloritoid from different metamorphic terrains worldwide (Figure 5.7). In order to evaluate the role of the bulk rock chemistry on the chemical composition of chloritoid, literature studies reporting both bulk rock composition and chloritoid chemistry have been selected.

5.3.1 Binary diagrams of chloritoid crystals in sample 11 and sample 13

A careful evaluation of potential chemical zoning within chloritoid crystals has been conducted using binary diagrams and short chemical profiles across chloritoid crystal. Firstly, core and rim compositions (Figure 5.11a-b) and “pale” and “dark” shades (Figure 5.11c-d) visible in the backscattered images (Figure 5.13– 5.15) are plotted in Al – X_{Mg} binary plots, where Al is plotted in atoms per formula unit (a.p.f.u.). Overall, in both samples there is no clear core-to-rim chemical zoning composition as well as between the pale and dark domains identified in the backscattered images.

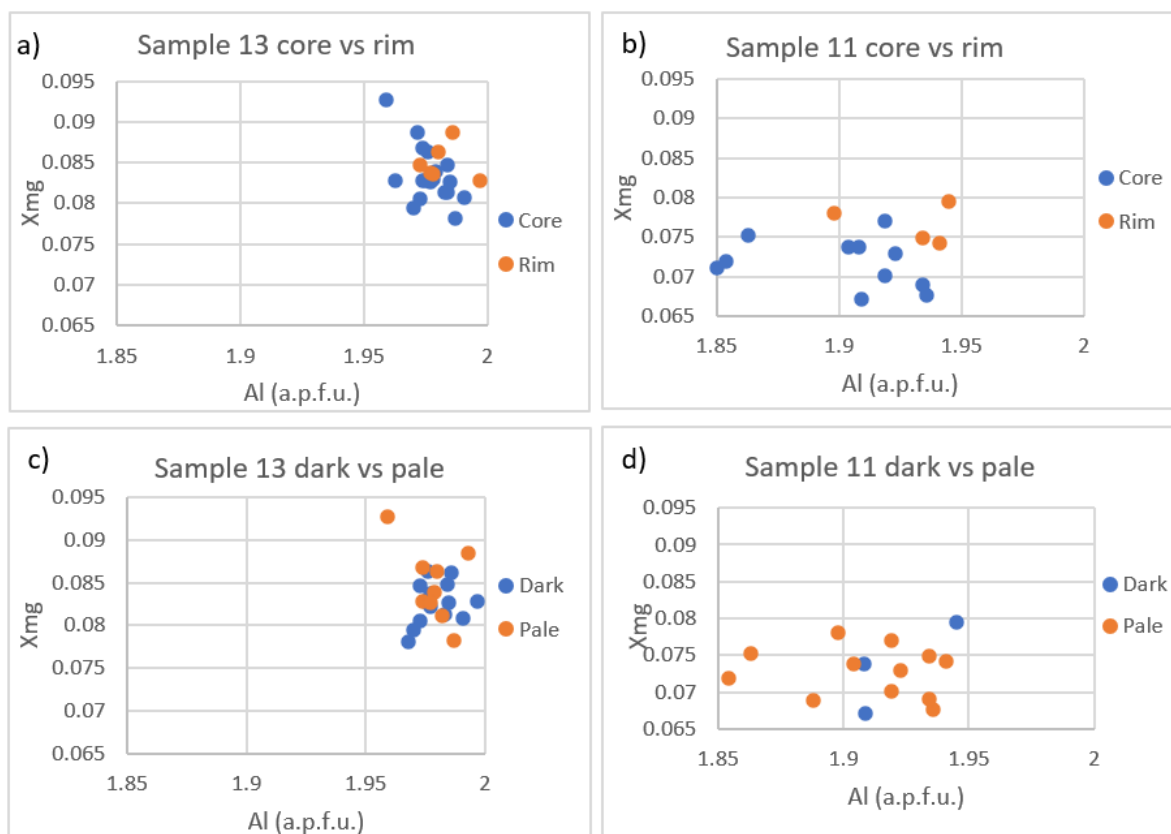


Figure 5.11 Binary diagrams plotting the ratio between X_{Mg} and Al (a.p.f.u.) in sample 11 and 13. 5.11a-b shows the points as either core or rim. 5.11c-d divides the points into pale or dark layer.

In the diagrams below (Figure 5.12), Al^{3+} is plotted against $\text{Ti}^{4+} + \text{Fe}^{3+}$ in order to evaluate the presence of a couple substitution between these elements. A linear trend, suggesting the occurrence of this substitution, is observed in the chloritoid from sample 11, whereas chloritoid from sample 13 does not show any trend.

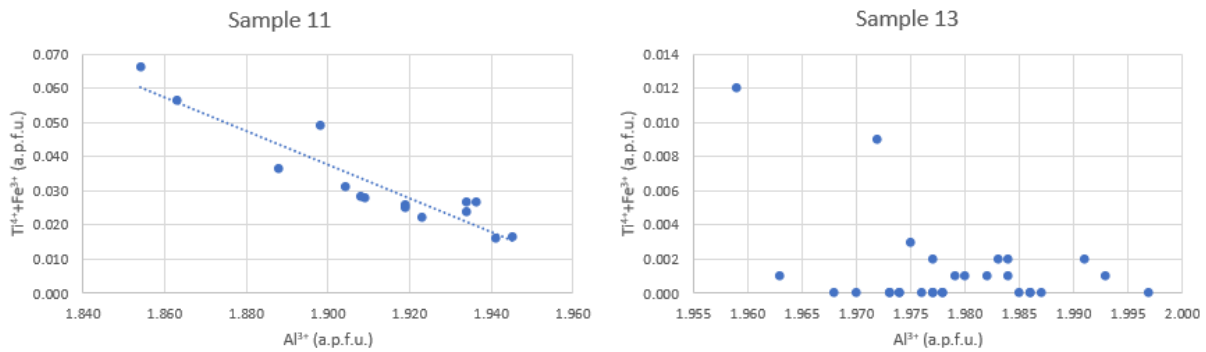


Figure 5.12. Binary diagrams plotting the $\text{Ti}^{4+} + \text{Fe}^{3+}$ against Al^{3+} in sample 11 and 13.

Punctual analyses profiles were also conducted through selected chloritoid crystals in order to evaluate the presence of chemical zoning (Figure 5.13 – 5.15).

In the chloritoid crystal 11a-S1 (Figure 5.13) from sample 11, X_{Mg} shows no correlation between core and rim whereas Al is slightly more enriched in the rims (1.909-1.945 a.p.f.u. in the rims and 1.850-1.888 a.p.f.u. in the core).

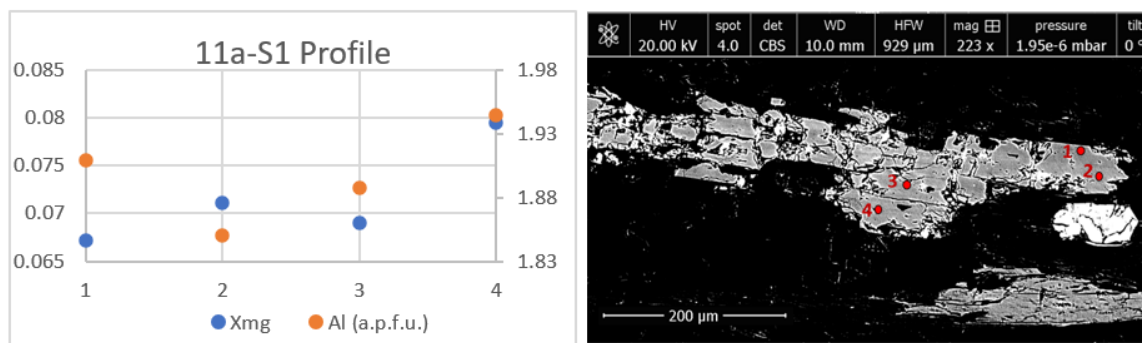


Figure 5.13. Compositional profile (X_{Mg} and Al) for chloritoid 11a-S1 crystal from sample 11 from this study. The SEM image to the right shows the location of the spot analyses in the crystal. Point 1 and 4 are interpreted as rim and 2 and 3 as core.

Chloritoid crystal 13-S2 (Figure 5.14) from sample 13 is characterised by an alternation of thin dark and pale grey domains in the backscattered image. This crystal is very fractured, and it is difficult to identify the original rims. The Al content is quite constant, with the exception of analysis 4, which displays low Al content (Al = 1.939 a.p.f.u.). X_{Mg} has no significant variation across the crystal, varying from 0.079-0.083 in the core to 0.078-0.088 in the rim. X_{Mg} is increasing through the profile.

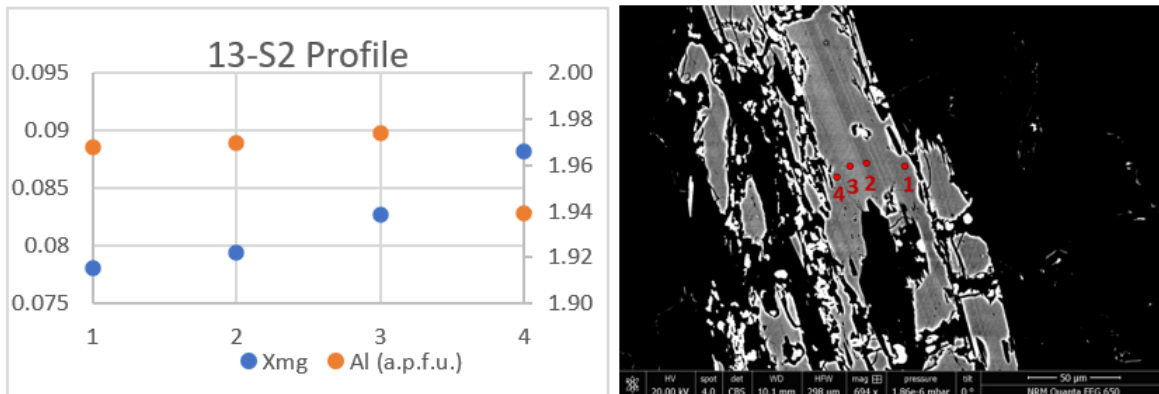


Figure 5.14. Compositional profile (X_{Mg} and Al) for chloritoid crystal from sample 13 from this study. The SEM image to the right shows the location of the spot analyses. Point 1 and 4 are interpreted as rim and 2 and 3 as core.

Chloritoid crystal 13-S8 (Figure 5.15) from sample 13 shows a slight increase in X_{Mg} from core to rim, (X_{Mg} = 0.081-0.83 core and X_{Mg} = 0.086-0.088 rim). Al displays a similar trend, although not as clear (Al= 1.977-1.991 a.p.f.u. core and Al= 1.986-1.993 a.p.f.u rim).

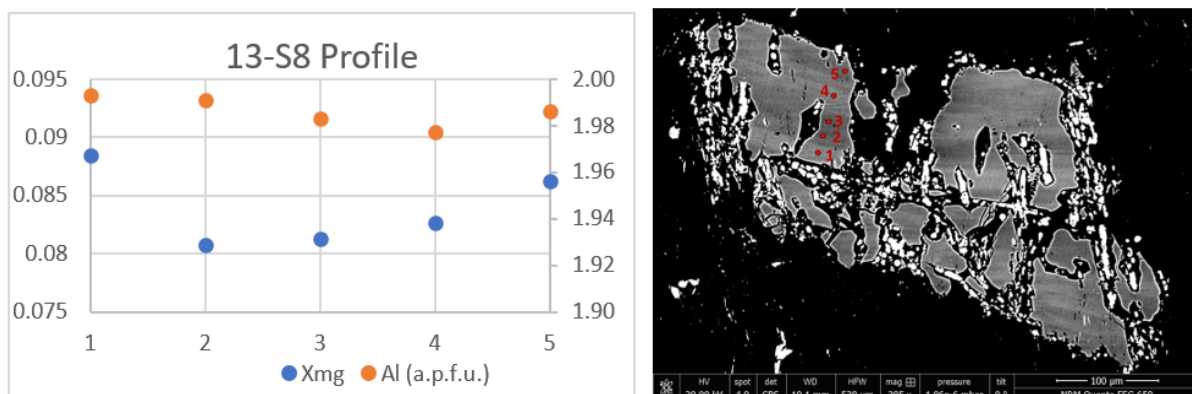


Figure 5.15. Compositional profile (X_{Mg} and Al) for chloritoid crystal from sample 13 from this study. The SEM image to the right shows the location of the spot analyses. Points 1 and 5 are interpreted as rim and points 2, 3 and 4 as core.

5.3.2 Chloritoid chemistry (samples 11 and 13)

The Fe^{2+} -Mg-Mn ternary diagrams (Figure 5.16) show that the chemical composition of chloritoid in samples 11 and 13 is rather similar, with respect to their Fe^{2+} -Mg-Mn ratio. The chloritoid in both samples is Mn-poor (Mn= 0-0.003 a.p.f.u. for sample 11; Mn= 0.006-0.011 a.p.f.u. for sample 13) and Fe-rich (Fe^{2+} = 0.91-0.96 a.p.f.u for sample 11 and Fe^{2+} = 0.89-0.92 a.p.f.u. for sample 13). The Mg content varies between 0.07-0.08 a.p.f.u. in sample 11 and between 0.08-0.09 in sample 13.

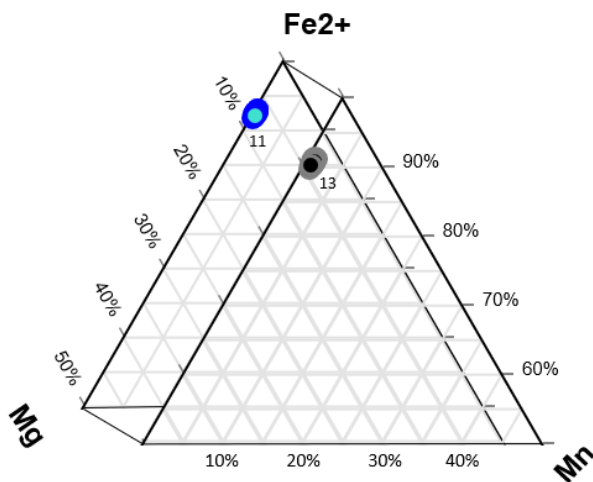


Figure 5.16. Fe^{2+} -Mg- Mn ternary diagrams showing the composition of chloritoid in samples 11 (blue) and 13 (black). The diagrams are cut at 50%.

If looking instead at the Fe^{2+} -Mg- Fe^{3+} ternary diagram (Figure 5.17), chloritoid in sample 13 commonly does not contain Fe^{3+} : the $\text{Fe}^{3+}/\text{Fe}^*$ ratio of chloritoid is generally equal to 0, with the exception of four analyses with a Fe_2O_3 value ranging between 0.003 and 0.067. By contrast, chloritoid in sample 11 displays Fe^{3+} up to 0.13 a.p.f.u. In this sample, the $\text{Fe}^{3+}/\text{Fe}^*$ is quite variable in chloritoid and ranges between 0 and 0.12. Chloritoid in sample 11 displays slightly lower Mg content (0.07-0.08 a.p.f.u.) than in sample 13 (0.08-0.09 a.p.f.u.). The same difference is observed for X_{Mg} of chloritoid, where sample 11 is slightly lower in X_{Mg} than sample 13 (0.07-0.08 in sample 11 and 0.08-0.09 in sample 13).

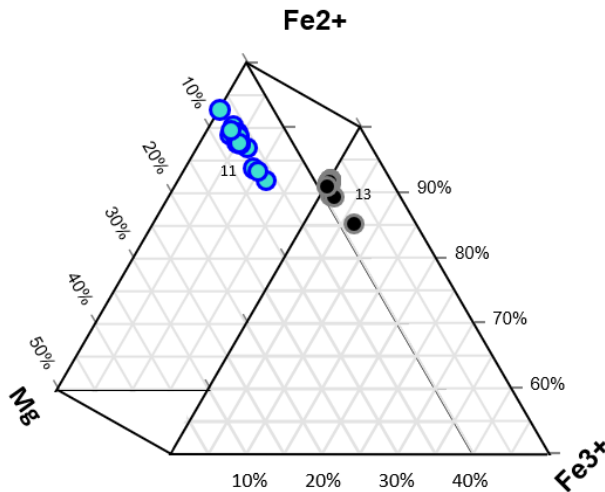


Figure 5.17. Fe^{2+} -Mg- Fe^{3+} ternary diagrams showing the composition of chloritoid in samples 11 (blue) and 13 (black). The diagrams are cut at 50%.

5.3.3 Chloritoid chemistry from literature review

The chemical compositions of chloritoid taken from the literature have been investigated in the diagrams below. Data are plotted using the same colour code and symbols as in Figure 5.8. In a few cases, chloritoid chemistry from studies with no bulk rock data is also plotted. Chloritoid chemical compositions from each study are first plotted separately. Then they are plotted together according to the groups defined on the basis of the bulk rock compositions (i.e. Group 1, Group 2a, Group 2b, Group 3; Figure 5.8-5.10).

Saih Hatat

Rocks of the Saih Hatat region in Oman (Figure 5.18) display chloritoids rich in Fe^{2+} and poor in Fe^{3+} (0 a.p.f.u. El-Shazly et al. 1995; 0.02-0.09 a.p.f.u. Agard et al. 2010). The same range is given for the $\text{Fe}^{3+}/\text{Fe}^*$ ratio (0 a.p.f.u. El-Shazly et al. 1995; 0.02-0.09 a.p.f.u. Agard et al. 2010). The samples are also Mn poor (median 0.005). The X_{Mg} of chloritoid is 0.06-0.11 (El-Shazly et al. 1995) and 0.09-0.12 (Agard et al. 2010), respectively. A comparison between the chloritoid chemistry of these literature studies and the ones investigated in this study reveals

that overall, the chloritoid in sample 13 displays a chemical composition similar to the one reported by Agard et al. (2010). By contrast, the chloritoid from El-Shazly et al. (1995) is poorer in Fe^{3+} .

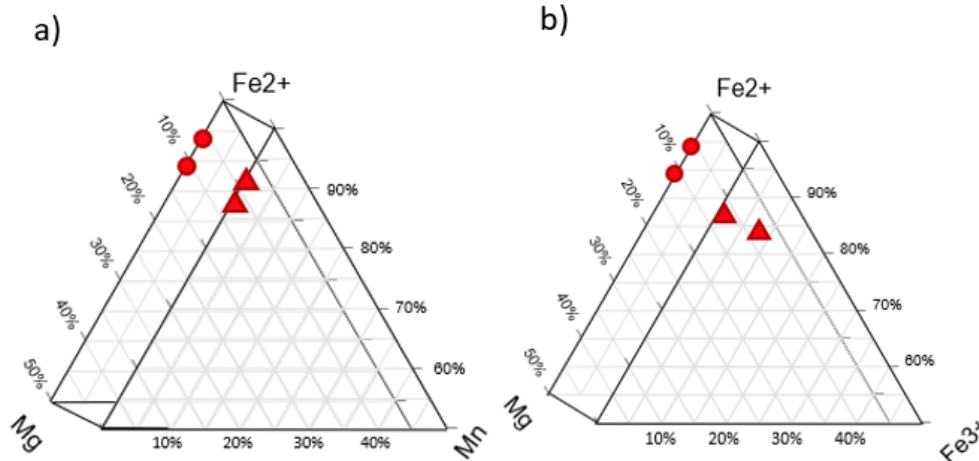


Figure 5.18. Fe^{2+} -Mg- Mn ternary diagrams (a) and Fe^{2+} - Mg- Fe^{3+} ternary diagrams (b) showing the composition of chloritoid in samples from Saih Hatat, Oman. The data is taken from El-Shazly (1995) (circles) and Agard et al. (2010) (triangles). The diagrams are cut at 50%.

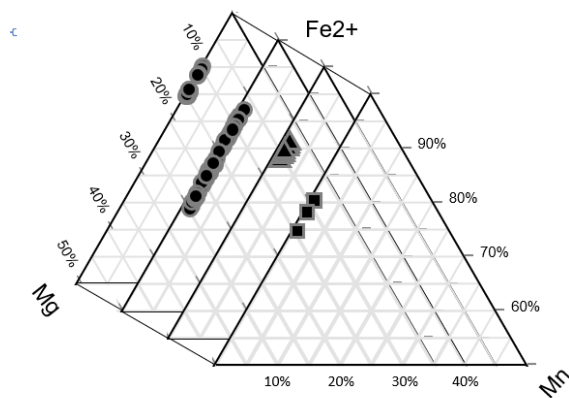
Apennines

Ternary plots reporting the chemical composition of chloritoid from the Apennines are shown in Figure 5.19. Chloritoid from the Apennines are generally Mn-poor (median 0.008 a.p.f.u.) and display a large chemical variability in terms of Mg and Fe^{2+} content. In some samples, chloritoid displays a relatively small chemical variability in terms of Fe^{2+} and Mg content (e.g. black triangles in Figure 8a, Lo P and Braga 2014). By contrast, chloritoid in other samples are characterised by a large variation in Fe^{2+} and Mg content (e.g. black circles, Papeschi et al. 2022; Figure 13a – sample R17).

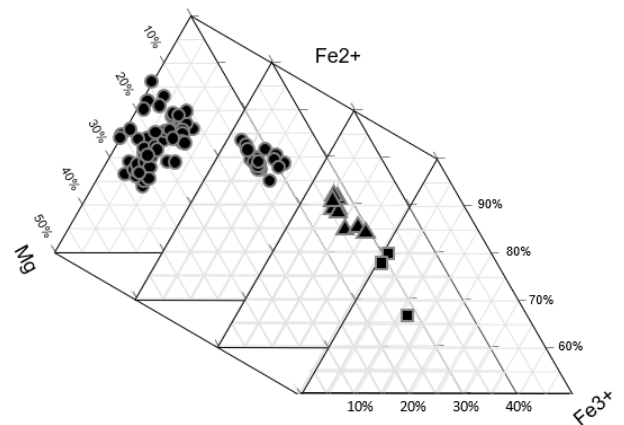
Chloritoids from the Apennines are commonly rich in Fe^{2+} (Figures 5.19a and c; Fe^{2+} up to 0.96 a.p.f.u., with a median of 0.82). Their X_{Mg} ranges between 0.10 and 0.30. Chloritoid from a kyanite-bearing sample investigated by Papeschi et al. 20203 represents an exception to this general trend (Fe^{2+} : 0.57-0.77 a.p.f.u.; X_{Mg} : 0.21-0.40).

With respect to their Fe^{3+} content, the Fe^{2+} - Fe^{3+} -Mg diagram (Figure 5.19b) shows that chloritoid from the Apennines generally contains Fe^{3+} (up to 0.17 a.p.f.u., Lo Po and Braga 2017). An exception is represented by the chloritoid from Papeschi et al. (2023), which is Fe^{3+} poor (Fe^{3+} 0–0.03 a.p.f.u.; Figure 5.19d).

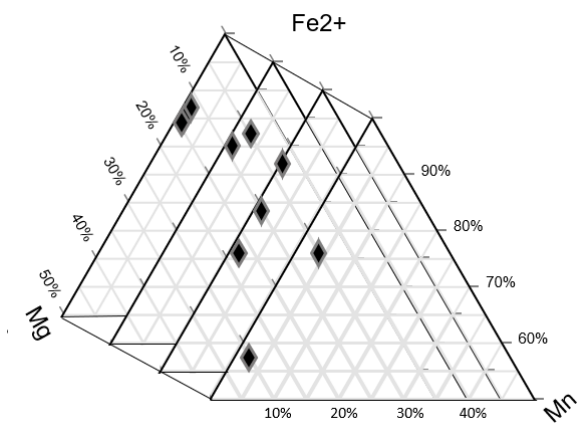
a)



b)



c)



d)

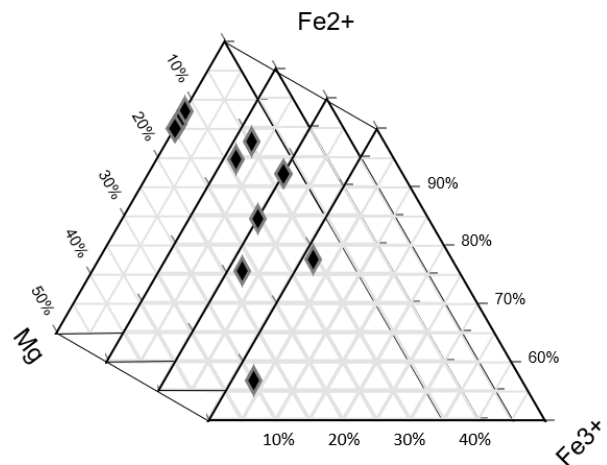
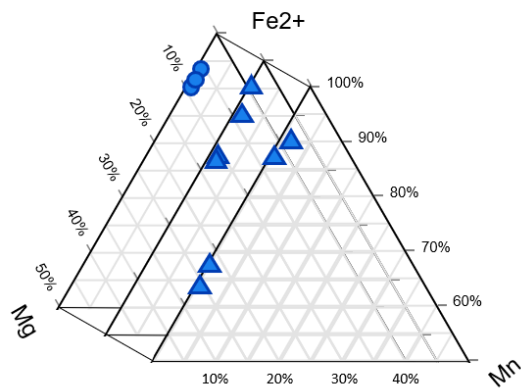


Figure 5.19. Fe^{2+} -Mg- Mn ternary diagrams (a, c) and Fe^{2+} - Mg- Fe^{3+} ternary diagrams (b, d) showing the composition of chloritoid in samples from the Apennines. The data is taken from Papeschi et al. (2022) with two separate samples, R6 and R17 (circles), Lo Po and Braga (2014) (triangles), Giuntoli et al. (2021) (squares) and Papeschi et al. (2023) with four separate samples (diamonds). The diagrams are cut at 50%.

Crete

The chloritoid from Crete studied by Seidel and Okrusch (1975) is Fe²⁺-rich (0.91-0.93 a.p.f.u.) and Mn- and Fe³⁺-poor (blue circles in Figures 14a and b). By contrast, in the samples investigated by Theye et al. (1992), chloritoid is Mn-poor, but displays a large variability in terms of Fe²⁺ and Mg content (Figure 5.20a, blue triangles) Its Fe³⁺ is generally low, except for a single analysis characterised by high Fe³⁺ (0-0.26 a.p.f.u.).

a)



b)

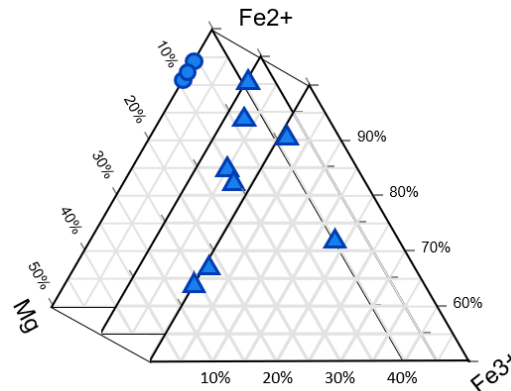
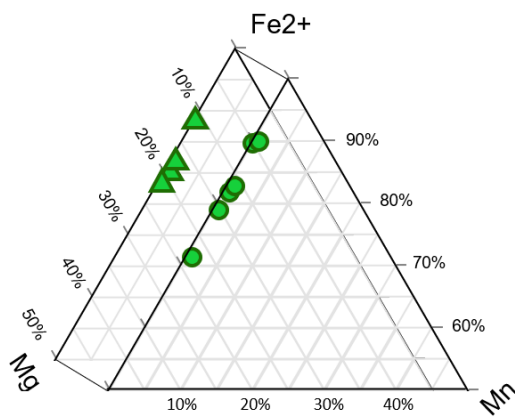


Figure 5.20. Fe²⁺-Mg- Mn ternary diagrams (a) and Fe²⁺- Mg- Fe³⁺ ternary diagrams (b) showing the composition of chloritoid in samples from Crete, Greece. The data is taken from Seidel and Okrusch (1975) (circles) and Theye et al. (1992) with two separate samples (triangles). The diagrams are cut at 50%.

Anatolia

The chloritoid investigated in the rocks from Anatolia, Turkey is Mn-poor and shows a large variation in its Fe²⁺ and Mg content (Figure 5.21a; X_{Mg}:0.04-0.17 green triangles from Candan et al. 2005; X_{Mg}:0.06-0.09 green circles from Pourteau et al. 2014). While chloritoid investigated by Candan et al. 2005 is Fe³⁺-free (green triangle in Figure 5.21b), the chloritoid from Pourteau et al. 2014 (green circles in Figure 5.21b) displays a variable content of Fe³⁺ content (Fe³⁺:0-0-09 a.p.f.u.).

a)



b)

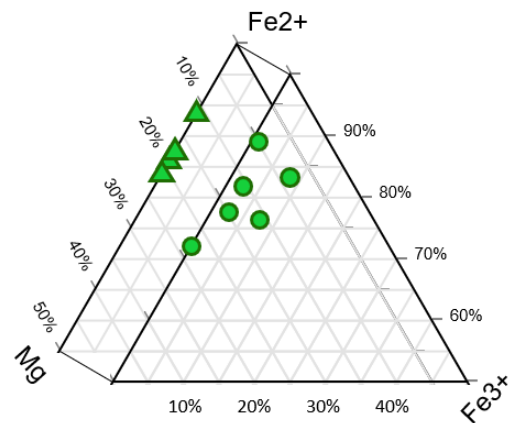
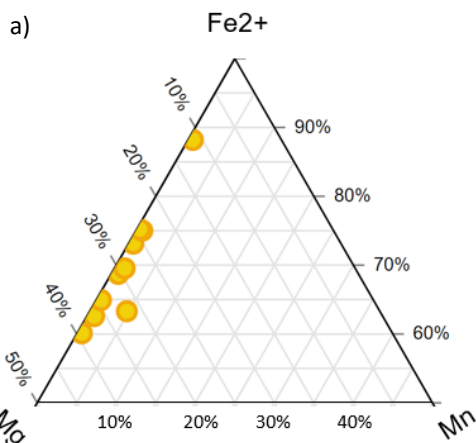


Figure 5.21. Fe^{2+} -Mg- Mn ternary diagrams (a) and Fe^{2+} - Mg- Fe^{3+} ternary diagrams (b) showing the composition of chloritoid in samples from the Anatolia, Turkey. The data is taken from Candan et al. (2005) (triangles) and Pourteau et al. (2014) (circles). The diagrams are cut at 50%.

Betic Cordillera

The chloritoids from southern Spain (Figure 5.22) are Mn-poor and display a large variability in their Mg and Fe^{2+} content (X_{Mg} is 0.11-0.40). They are poor in Fe^{3+} (0-0.04 a.p.f.u.).



b)

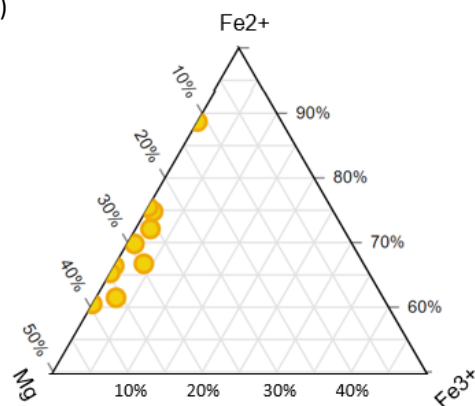
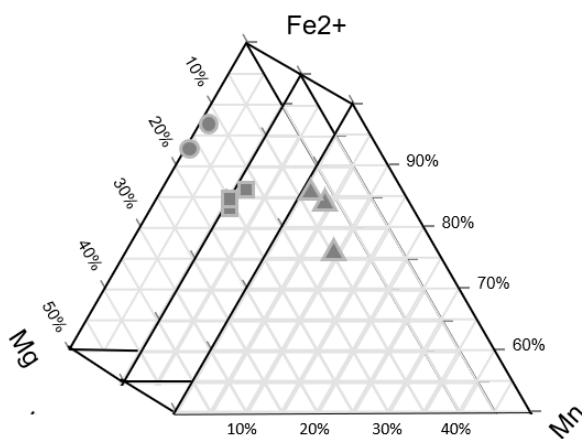


Figure 5.22. Fe^{2+} -Mg- Mn ternary diagrams (a) and Fe^{2+} - Mg- Fe^{3+} ternary diagrams (b) showing the composition of chloritoid in samples from the Betic Cordillera, Spain. The data is taken from Azanon and Goffé (1997). The diagrams are cut at 50%.

Alps

Chloritoid from the Alps (Figure 5.23) (Agard et al., 2001, Plunder et al. 2012) displays a similar composition to the one from the Apennines. An exception is represented by chloritoid investigated by Bousquet et al. (2022) which is characterised by higher Mn content (0.01-0.08 a.p.f.u.). Chloritoid from the Alps commonly contain a low Fe^{3+} content (< 0.05 a.p.f.u.) and its $\text{Fe}^{3+}/\text{Fe}^*$ ratio is in the range 0-0.07. The X_{Mg} is comprised between 0.12 and 0.21.

a)



b)

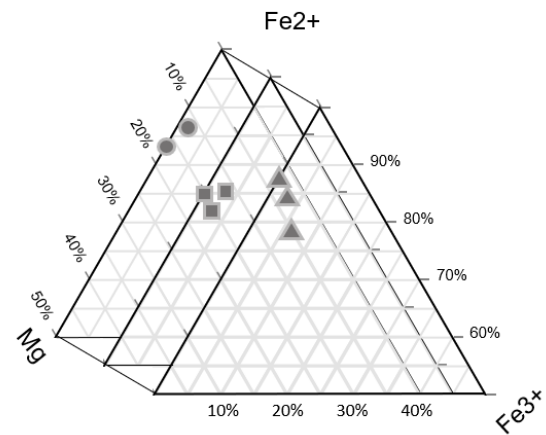
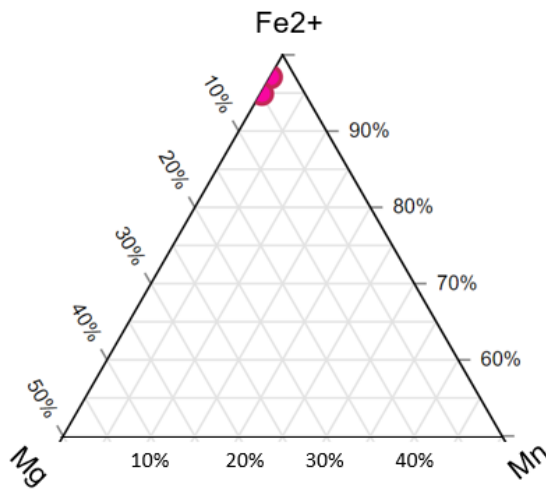


Figure 5.23. Fe^{2+} -Mg- Mn ternary diagrams (a) and Fe^{2+} - Mg- Fe^{3+} ternary diagrams (b) showing the composition of chloritoid in samples from the Alps. The data is taken from Agard et al. (2001) (circles), Plunder et al. (2012) (squares) and Bousquet et al. (2022) (triangles). The diagrams are cut at 50%.

Calabride complex

Chloritoid from the Calabride complex (Figure 5.24) is Mn- and Mg-poor ($\text{Mg} < 0.05$ a.p.f.u.; X_{Mg} : 0.03-0.05) and rather Fe^{3+} -rich (0.06-0.09 a.p.f.u.). Its $\text{Fe}^{3+}/\text{Fe}^*$ ratio is in the range 0.06-0.09.

a)



b)

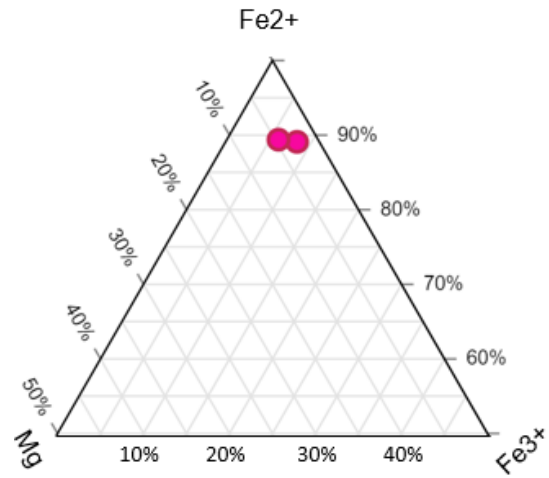


Figure 5.24. Fe^{2+} -Mg- Mn ternary diagrams (a) and Fe^{2+} - Mg- Fe^{3+} ternary diagrams (b) showing the composition of chloritoid in samples from the Calabride complex, Italy. The data is taken from Rosetti et al. (2004). The diagrams are cut at 50%.

In the following, chloritoid compositions are plotted with respect to the Groups defined on the basis of the bulk rock compositions.

Group 1

Group 1 has the highest Al_2O_3 bulk composition in the AFM diagram (Figure 5.8). The Fe^{2+} -Mg-Mn diagram (Figure 5.25a) shows that the chloritoid from Group 1 is Mn-poor but displays a wide range in terms of Fe^{2+} and Mg content. The Fe^{2+} -Mg- Fe^{3+} diagram (Figure 5.25b) shows that the Fe^{3+} distribution is broad as well, but that most of the analyses do not display Fe^{3+} . The maximum content of Fe^{3+} is 0.111 a.p.f.u.

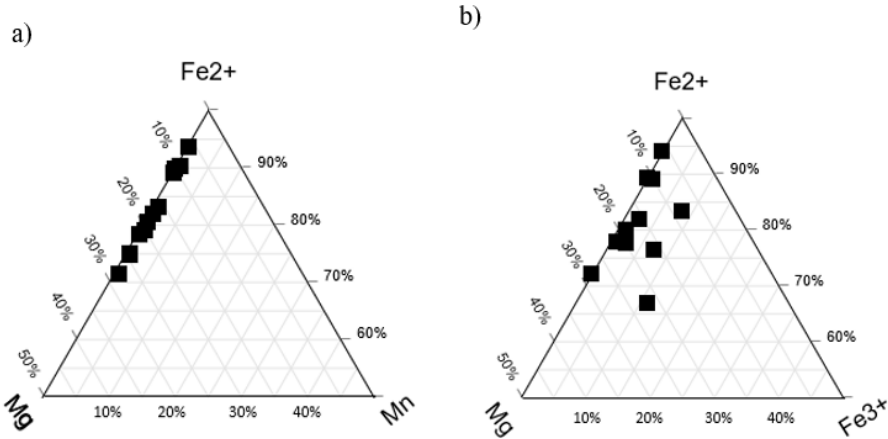


Figure 5.25. Fe²⁺-Mg- Mn ternary diagrams (a) and Fe²⁺- Mg- Fe³⁺ ternary diagrams (b) showing the composition of chloritoid in Group 1 from Figure 2. The diagrams are cut at 50%.

Group 2a

Group 2a (Figure 5.26) is categorized by intermediate Al₂O₃ content in the AFM diagram (Figure 5.8) and high FeO content (Figure 5.9 and 5.10). Chloritoid belonging to this group is Mn-poor and is generally Fe²⁺ rich, with a few analyses rich in Mg. Its Fe³⁺ content is generally low, with a few exceptions (Fe³⁺ content up to 0.264 a.p.f.u).

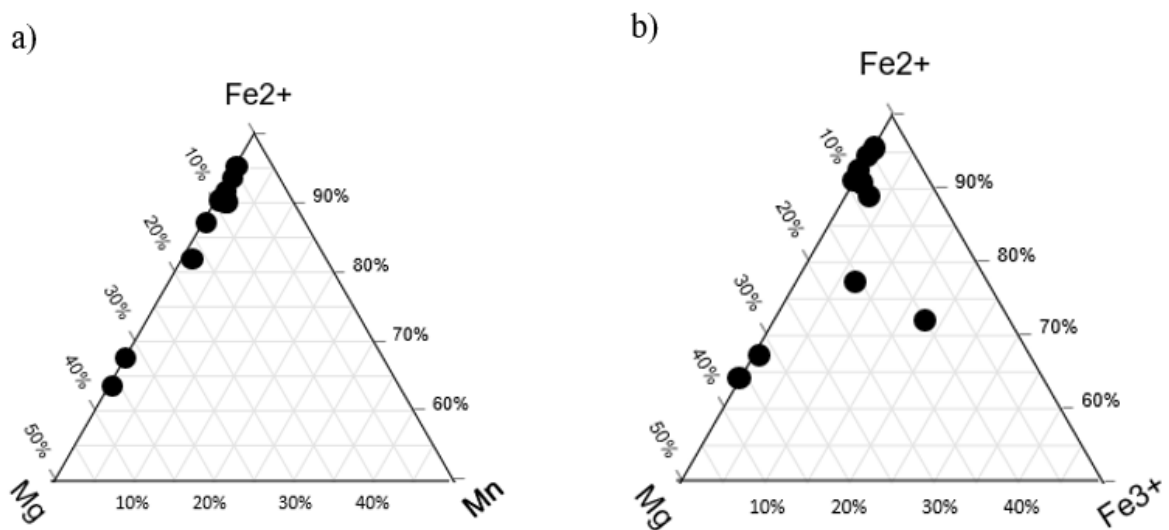


Figure 5.26. Fe²⁺-Mg- Mn ternary diagrams (a) and Fe²⁺- Mg- Fe³⁺ ternary diagrams (b) showing the composition of chloritoid in Group 2a from Figure 3 and 4. The diagrams are cut at 50%.

Group 2b

Group 2b (Figure 5.27) is categorized as intermediate Al_2O_3 in the AFM diagram projected from muscovite, quartz and H_2O (Figure 5.8) and displays a higher Fe_2O_3 content than Groups 1 and 2a (Figure 5.8 and 5.9). Similar to the chloritoid belonging to Groups 1 and 2a, the Mg and Fe^{2+} content of chloritoid of Group 2b is quite variable. In this group, chloritoid displays slightly higher Mn content (Mn up to 0.036 a.p.f.u) than in the previous group. The most striking feature is the presence of Fe^{3+} in chloritoid (Fe^{3+} up to 0.131 a.p.f.u.; Figure 5.27b).

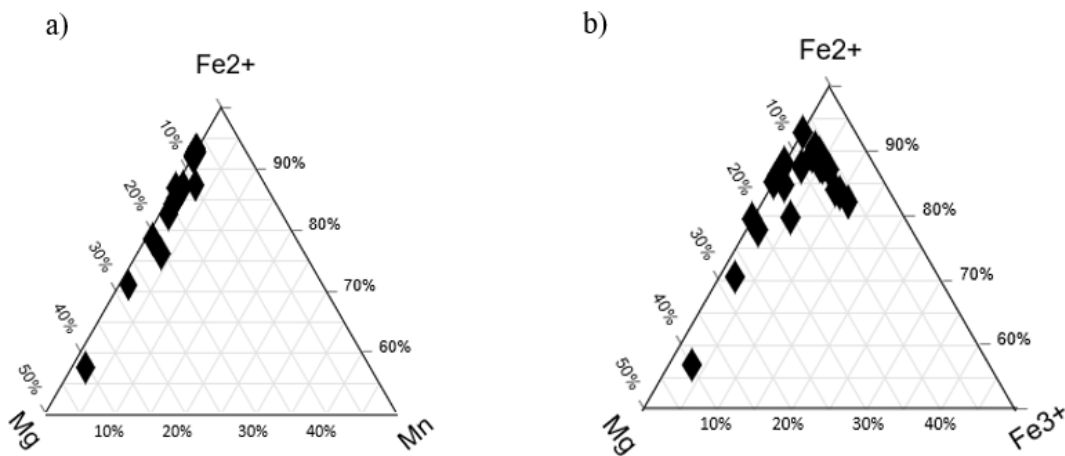


Figure 5.27. Fe^{2+} -Mg- Mn ternary diagrams (a) and Fe^{2+} - Mg- Fe^{3+} ternary diagrams (b) showing the composition of chloritoid in Group 2b from Figure 3 and 4. The diagrams are cut at 50%.

Group 3

Group 3 (Figure 5.28) contains the lowest Al_2O_3 content in the AFM diagram (Figure 5.8) and the highest Fe_2O_3 content (Figures 5.9-5.10). The chloritoid belonging to this group is Mn-poor and displays a smaller variability in terms of Mg and Fe^{2+} content (Figure 5.28a) compared to the other groups. Chloritoid is generally Fe^{2+} rich (X_{Mg} : 0.078-0.160). Its Fe^{3+} is quite variable, but most of the analyses displays some Fe^{3+} (Fe^{3+} up to 0.143 a.p.f.u.).

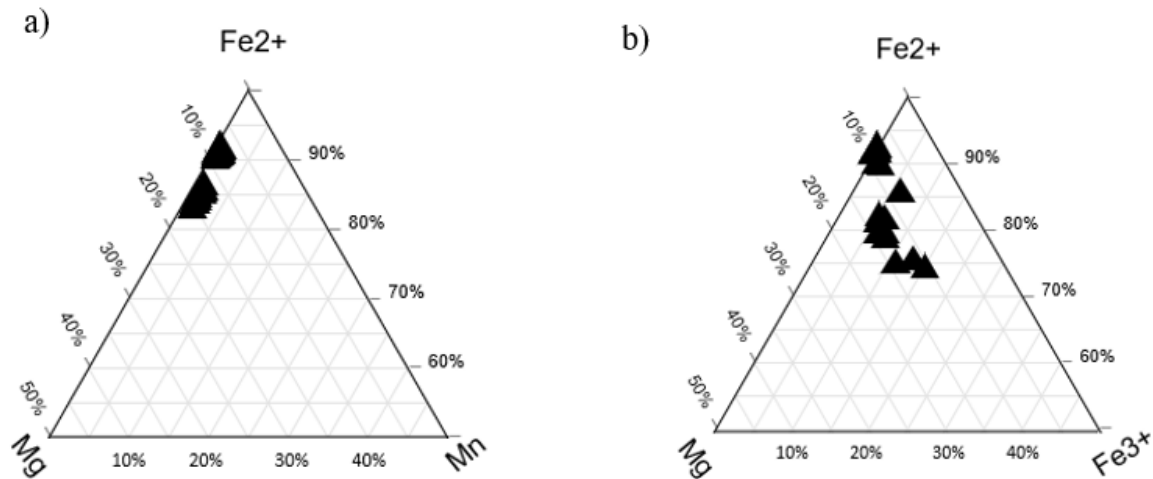


Figure 5.28. Fe²⁺-Mg- Mn ternary diagrams (a) and Fe²⁺- Mg- Fe³⁺ ternary diagrams (b) showing the composition of chloritoid in Group 3 from Figure 3 and 4. The diagrams are cut at 50%.

6. DISCUSSION

6.1 Chloritoid occurrences in the Saih Hatat window (Oman)

Samples 11 and 13 are chloritoid-bearing metapelites from the Saih Hatat Window (Oman) and they were carefully investigated in this study. According to previous studies (e.g. Yamato et al., 2007), this Unit reached 0.7-0.9 GPa and 400-460°C. The two samples display a similar mineralogy, mainly consisting of quartz, white mica and chloritoid. However, a few important mineralogical differences between them should be highlighted. Firstly, chloritoid is very rare in sample 11 (only a few crystals have been identified). Secondly, sample 13 displays a large modal amount (~20%) of Fe³⁺ oxides and hydroxides, namely hematite (Fe₂O₃) and goethite (Fe³⁺O(OH)). The latter are mainly concentrated in layers oriented parallel to the foliation, but they also strongly replace chloritoid. Other differences consist in the presence of chlorite and ankerite in sample 11 and of graphite in sample 13.

With respect to their bulk-rock composition, both samples display relatively low Fe₂O₃* (1.97 wt.% and 3.00 wt.%, respectively), but show a significant difference in their bulk Fe³⁺/Fe* (0.34 in sample 11 and 0.77 in sample 13). Another remarkable difference between the two samples is their Al₂O₃ content: sample 11 is Al-poor (2.63 wt.%) whereas sample 13 is Al-rich (14.42

wt.%). The low Al₂O₃ content of sample 11 is considered as the main factor for the low modal amount of chloritoid observed in this sample.

Chloritoid in the two samples not only is present in different modal amount, but also displays different chemistry. Chloritoid in sample 11 commonly contains Fe³⁺ and displays a maximum Fe³⁺/Fe* of 0.12. By contrast, chloritoid in sample 13 generally does not show Fe³⁺ and only a few analyses contain a limited Fe³⁺ content resulting in a maximum Fe³⁺/Fe* of 0.07.

In sample 13, the high bulk Fe³⁺/Fe* and the absence of Fe³⁺ in chloritoid may be explained by an intense oxidation stage affecting the rock after the growth of chloritoid. This process was also responsible for a pervasive and widespread replacement of chloritoid by hematite and minor goethite. Therefore, in sample 13 it is not possible to evaluate a potential link between the bulk Fe³⁺/Fe* and the chemistry (in particular with respect to its Fe³⁺) of chloritoid.

6.1.1 Oxidation of Oman rocks

The rocks exposed in the Saih Hatat (Oman) display various degree of oxidation and an increase of this process has been recognised from south to north of Saih Hatat (Goffé et al., 1988). According to Goffé et al. (1988), metamorphic rocks from Oman underwent oxidation during cooling as a consequence of hydrothermalism (Goffé et al., 1988). However, the exact timing of oxidation remains unconstrained and more recent studies identified Cretaceous as well as ongoing meteoric weathering as the main cause of the present degree of oxidation shown by Oman rocks (e.g. Miller et al., 2016).

More generally, iron-rich minerals such as chloritoid, chlorite and carpholite reacted together with H₂O and/or O to form kaolinite and iron oxides. The main chemical reactions involving these minerals are:

- 1) $\text{Cld} + \text{Qz} + \text{H}_2\text{O} + \text{O}_2 \rightarrow \text{Kln} + \text{Fe-oxide}$
- 2) $\text{Fe-Chl} + \text{O}_2 \rightarrow \text{Kln} + \text{Fe-oxide} + \text{Qz} + \text{H}_2\text{O}$
- 3) $\text{Fe-Car} + \text{O}_2 + \text{H}_2\text{O} \rightarrow \text{Kln} + \text{Fe-oxide}$

Different Fe-oxides can develop within the same metamorphic setting (Holland and Worley, 2000). Thermodynamic models indicate that the stability field of Fe³⁺- bearing minerals increases at increasing Fe³⁺ in the system (Warren and Waters, 2006). Sample 13 investigated

in this study is characterised by a higher modal amount of Fe^{3+} -oxides than sample 11, suggesting that it was affected by an intense oxidative weathering.

6.1.2 Chloritoid zonation in sample 11 and 13

Some studies have reported chemical zonation in chloritoids (e.g. Yamato et al., 2007; Pourteau et al., 2014), however the chloritoid-bearing samples investigated in this study lack any signs of zonation. The X_{Mg} variation in the chloritoids show a narrow range from 0.07-0.08 and 0.08-0.09 for sample 11 and 13, respectively. By contrast, on close inspection by scanning electron microscope (Figure 5.13-5.15) reveals network of thin fractures along which chloritoid is partially dissolved. Along these fractures, chloritoid is heavily replaced by oxides.

6.2 Chloritoid occurrences in metapelites: bulk-rock chemical control

The bulk compositions of chloritoid-bearing samples and the chemistry of chloritoid from other metamorphic terrains worldwide have been compared to the ones of the two samples of the Hulw Unit investigated in this study (from the Saih Hatat Window). This comparison aims to assess if there is a potential link between the Fe^{3+} bulk content and the Fe^{3+} content of chloritoid. As explained above, the bulk composition of sample 13 cannot be used for this purpose because it was altered by oxidation and thus it will not be considered. In all reviewed samples, the $\text{Fe}^{3+}/\text{Fe}^*$ ratio is systematically higher in the bulk than in chloritoid ($\text{Fe}^{3+}/\text{Fe}^* < 0.2$), indicating that Fe^{3+} is less compatible in chloritoid compared to other minerals in chloritoid-bearing rocks, especially Fe-rich oxides. In Figure 6.1, the reviewed samples are groups based on their main mineral assemblages. All samples contain quartz and white mica, hereafter referred to as (+ Qz + Wm). The samples without hematite will be discussed first followed by a brief analysis on the hematite bearing samples.

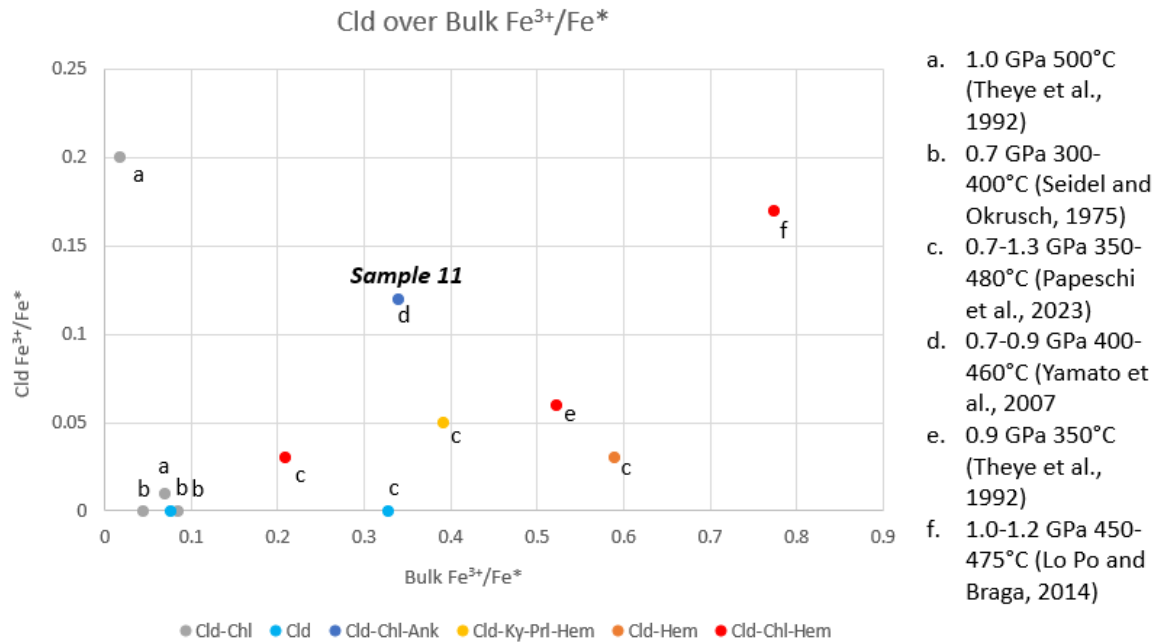


Figure 6.1. Binary diagram displaying the Fe³⁺/Fe* ratio of the bulk and chloritoid for sample 11 and for data from literature review. The colours used for the dots refer to the peak mineral assemblage. The latter also includes quartz and white mica. The letters refer to different P-T conditions estimated for the investigated samples. The P-T conditions of sample 11 are from Yamato et al (2007).

The metapelites containing chloritoid – chlorite (Qz+ Wm) (grey circles in figure 6.1) display a low bulk Fe³⁺/Fe* (bulk Fe³⁺/Fe* <0.1) and chloritoid is generally Fe³⁺-poor (Fe³⁺/Fe* < 0.05). There is only one sample in which chloritoid displays a slightly higher Fe³⁺/Fe* (~0.2). This “outlier” is sample K76/107 from Crete (Theye et al.,1992). Interestingly, the authors reported the presence of pyrophyllite in this sample, but they were quite imprecise in estimating its modal amount (in the range 2-20 vol.%, Table 2 in Theye et al. 1992). Therefore, it is difficult to draw some conclusions using this sample.

Metapelites containing the mineral assemblage chloritoid (+Qz +Wm) (light blue circles in Figure 6.1) show a higher bulk Fe³⁺/Fe* (up to ~0.33) but chloritoid does not contain Fe³⁺.

Metapelites containing the mineral assemblage chloritoid – kyanite – pyrophyllite – hematite (+ Qz + Wm) (yellow circle in Figure 6.1) display a moderate bulk Fe³⁺/Fe* (0.39) and a rather high Fe³⁺/Fe* (0.05) in chloritoid. The authors (Papeschi et al., 2023) have interpreted the presence of Fe³⁺ in chloritoid as the result of a high bulk Al₂O₃ content. The latter would have favoured the stabilization of Al-rich minerals (e.g. kyanite, pyrophyllite) that coexists with chloritoid, facilitating the incorporation of Fe³⁺ in chloritoid, due to the couple substitution Al³⁺ → Fe³⁺ + Ti⁴⁺.

Metapelites containing the mineral assemblage chloritoid – hematite (+ Qz + Wm) (orange circle in Figure 6.1) display a high bulk $\text{Fe}^{3+}/\text{Fe}^*$ of 0.59, but relatively low $\text{Fe}^{3+}/\text{Fe}^*$ (0.03) in chloritoid.

Metapelites containing the mineral assemblage chloritoid – chlorite – hematite (+ Qz + Wm) (red circles in Figure 6.1) are characterised by variable bulk $\text{Fe}^{3+}/\text{Fe}^*$ (0.21-0.78) and chloritoid $\text{Fe}^{3+}/\text{Fe}^*$ (0.04-0.17). Notably, there is a positive correlation between the bulk $\text{Fe}^{3+}/\text{Fe}^*$ and the $\text{Fe}^{3+}/\text{Fe}^*$ in chloritoid (i.e., the $\text{Fe}^{3+}/\text{Fe}^*$ in chloritoid increases at increasing bulk $\text{Fe}^{3+}/\text{Fe}^*$).

Sample 11 (blue circle in Figure 6.1) from this study contains the mineral assemblage chlorite – chloritoid – ankerite (+ Qz + Wm). It has an intermediate bulk $\text{Fe}^{3+}/\text{Fe}^*$ (0.34) but a rather high $\text{Fe}^{3+}/\text{Fe}^*$ ratio in the chloritoid (0.12). With respect to the literature bulk compositions plotted in this diagram, sample 11 differs for high SiO_2 and low Al_2O_3 contents and thus a direct comparison with the other plotted samples appears quite difficult. Nevertheless, some hypotheses can be generated based on the bulk and mineral chemistry of this sample. Chloritoid contains Fe^{3+} suggesting that the couple substitution $\text{Al}^{3+} \rightarrow \text{Fe}^{3+} + \text{Ti}^{4+}$ has taken place (see section 5.3.1 Figure 5.12). Therefore, it may be speculated that, despite the very low Al_2O_3 shown by this sample, the occurrence of chloritoid may have been favoured by a moderate bulk $\text{Fe}^{3+}/\text{Fe}^*$ (0.34).

On the basis of the literature review, a few observations can be drawn:

- The sample with the lowest bulk $\text{Fe}^{3+}/\text{Fe}^*$ (grey circle in Figure 6.1) is characterized by the mineral assemblage chloritoid – chlorite – pyrophyllite(?) (+ Qz + Wm). Chloritoid from this sample displays the highest $\text{Fe}^{3+}/\text{Fe}^*$, although all other samples with this mineralogy show chloritoid which is depleted in Fe^{3+} .
- The highest bulk $\text{Fe}^{3+}/\text{Fe}^*$ has been measured in a sample containing the mineral assemblage chloritoid – chlorite – hematite (+ Qz + Wm). Chloritoid from this sample also displays high $\text{Fe}^{3+}/\text{Fe}^*$ (red circle in Figure 6.1)

7. CONCLUSIONS

This thesis investigates the chloritoid occurrences in a few samples from the Saih Hatat window (Oman). The conclusions are as follow:

- If a metapelite is subjected to oxidation during weathering, chloritoid crystals are commonly altered and replaced by iron oxides, which incorporates a considerable amount of Fe^{3+} to the bulk composition. Sample 13 from this study is an excellent example of this process.
- Oxidation weathering cause a major problem when attempting to assess the relationship between $\text{Fe}^{3+}/\text{Fe}^*$ in the bulk and in the rock-forming minerals, such as chloritoid or amphibole. In order to properly evaluate this relationship, a focus on pristine chloritoid-bearing rocks, that have not been influenced by any later oxidation stage, would be considered.
- A high bulk $\text{Fe}^{3+}/\text{Fe}^*$ does not directly imply a high $\text{Fe}^{3+}/\text{Fe}^*$ in chloritoid. Instead, the coexisting minerals, as well as the Al_2O_3 and Fe_2O_3 content in the bulk play an important role in the stability and chemistry of chloritoid.

Acknowledgements

I would first and foremost like to thank my supervisor prof. Paola Manzotti for helping me understand and formulate my thesis thoroughly. I would also like to thank prof. Michel Ballèvre for his excellent microscopy input and Dr. Francesco Nosenzo for helping me with the SEM. I would like to thank prof. Uwe Ring for his input on my geological background, seeing as he is an expert in the structure and geology of Oman. I also want to thank his postdoc Reuben Hansman for his excellent paper on Oman and for taking his time to answer my questions. I also want to thank Andreas Scharf for collecting the samples I have worked with.

I would like to thank Jessica Langlade from the University of Western Brittany, for doing my microprobe (EMPA) measurements and to the SARM-CRPG lab in Nany for the XRF measurements.

Last but not least, I would like to thank my partner Vidar Jakobsson for his endless support and discussions. His thirst for knowledge inspires me every day. I also want to thank my sister Sylvia Morawiecki and my friends Mikaela Krona, Bella Dillan, and Elise Lindell for believing in me and always being there by my side.

References

- Agard, P., Searle, M. P., Alsop, G. I., & Dubacq, B. (2010). Crustal stacking and expulsion tectonics during continental subduction: P-T deformation constraints from Oman. *Tectonics*, 29(5).
- Arndt, N. T. (2013). The formation and evolution of the continental crust. *Geochemical Perspectives*, 2(3), 405-405.
- Bailey, E. H. (1981). Geologic map of Muscat-Ibra area, Sultanate of Oman. *Journal of Geophysical Research*, 86.
- Brouwer, P. (2006). Theory of XRF. *Almelo, Netherlands: Paralytical BV*.
- Carignan, J., Hild, P., Mevelle, G., Morel, J. & Yeghicheyan, D. (2001). Routine analyses of trace elements in geological samples using flow injection and low pressure on-line liquid chromatography coupled to ICP-MS: a study of geochemical reference materials, BR, DRN, UB-N, AN-G and GH. *Geostandards Newsletter* 25, 187–198.
- EL-SHAZLY, A. E. D. K. (1994). Petrology of lawsonite-, pumpellyite-and sodic amphibole-bearing metabasites from north-east Oman. *Journal of Metamorphic Geology*, 12(1), 23-48.
- EL-SHAZLY, A. E. D. K. (1995). Petrology of Fe-Mg-carpholite-bearing metasediments from NE Oman. *Journal of Metamorphic Geology*, 13(3), 379-396.
- El-Shazly, A. K., & Liou, J. G. (1991). Glaucophane chloritoid-bearing assemblages from NE Oman: petrologic significance and a petrogenetic grid for high P metapelites. *Contributions to Mineralogy and Petrology*, 107, 180-201.
- Ganguly, J. (1969). Chloritoid stability and related paragenesis; theory, experiments, and applications. *American Journal of Science*, 267(8), 910-944.
- Ganguly, J., & Newton, R. C. (1968). Thermal stability of chloritoid at high pressure and relatively high oxygen fugacity. *Journal of Petrology*, 9(3), 444-466.

- Giuntoli, F., & Viola, G. (2021). Cyclic brittle-ductile oscillations recorded in exhumed high-pressure continental units: A record of deep episodic tremor and slow slip events in the northern Apennines. *Geochemistry, Geophysics, Geosystems*, 22(9), e2021GC009805.
- Goffé, B., & Chopin, C. (1986). High-pressure metamorphism in the Western Alps: zoneography of metapelites, chronology and consequences. *Schweizerische mineralogische und petrographische Mitteilungen*, 66(1-2), 41-52.
- Goffé, B., Michard, A., Kienast, J. R., & Le Mer, O. (1988). A case of obduction-related high-pressure, low-temperature metamorphism in upper crustal nappes, Arabian continental margin, Oman: PT paths and kinematic interpretation. *Tectonophysics*, 151(1-4), 363-386.
- Hansman, R. J., Ring, U., Scharf, A., Glodny, J., & Wan, B. (2021). Structural architecture and Late Cretaceous exhumation history of the Saih Hatat Dome (Oman), a review based on existing data and semi-restorable cross-sections. *Earth-Science Reviews*, 217, 103595.
- Holland, T. J. B., & Powell, R. (1990). An enlarged and updated internally consistent thermodynamic dataset with uncertainties and correlations: the system K₂O–Na₂O–CaO–MgO–MnO–FeO–Fe₂O₃–Al₂O₃–TiO₂–SiO₂–C–H₂–O₂. *Journal of metamorphic Geology*, 8(1), 89-124.
- Holland, T. J. B., & Powell, R. T. J. B. (1998). An internally consistent thermodynamic data set for phases of petrological interest. *Journal of metamorphic Geology*, 16(3), 309-343.
- Holland, & Worley. (2000). The effect of TiO₂ and Fe₂O₃ on metapelitic assemblages at greenschist and amphibolite facies conditions: mineral equilibria calculations in the system K₂O–FeO–MgO–Al₂O₃–SiO₂–H₂O–TiO₂–Fe₂O₃. *Journal of Metamorphic Geology*, 18(5), 497-511.
- Jolivet, L., Faccenna, C., Goffé, B., Mattei, M., Rossetti, F., Brunet, C., ... & Parra, T. (1998). Midcrustal shear zones in postorogenic extension: example from the northern Tyrrhenian Sea. *Journal of Geophysical Research: Solid Earth*, 103(B6), 12123-12160.
- Klein, C., & Philpotts, A. R. (2017). *Earth materials: introduction to mineralogy and petrology*. Cambridge University Press.
- Lo Pò, D., & Braga, R. (2014). Influence of ferric iron on phase equilibria in greenschist facies assemblages: the hematite-rich metasedimentary rocks from the Monti Pisani (Northern Apennines). *Journal of Metamorphic Geology*, 32(4), 371-387.

- MacKenzie, W. S., Adams, A. E., & Brodie, K. H. (2017). *Rocks and minerals in thin section*. CRC Press.
- Manzotti, P., Ballèvre, M., Pitra, P., Putlitz, B., Robyr, M., & Müntener, O. (2020). The growth of sodic amphibole at the greenschist-to blueschist-facies transition (Dent Blanche, Western Alps): bulk-rock chemical control and thermodynamic modelling. *Journal of Petrology*, *61*(4), ega044.
- Michard, A., Bouchez, J. L., & Misseri, M. (1981). Les nappes métamorphiques de Mascate, nouvel élément infraophiolitique en Oman. *Terra Cognita*, *1*, 19.
- Miller, H. M., Matter, J. M., Kelemen, P., Ellison, E. T., Conrad, M. E., Fierer, N., ... & Templeton, A. S. (2016). Modern water/rock reactions in Oman hyperalkaline peridotite aquifers and implications for microbial habitability. *Geochimica et Cosmochimica Acta*, *179*, 217-241.
- Papeschi, S., Pontesilli, A., Romano, C., Rossetti, F., & Theye, T. (2022). Alpine subduction zone metamorphism in the Palaeozoic successions of the Monti Romani (Northern Apennines, Italy). *Journal of Metamorphic Geology*, *40*(5), 919-953.
- Papeschi, S., Rossetti, F., & Walters, J. B. Growth of kyanite and Fe-Mg chloritoid in Fe₂O₃-rich HP–LT metapelites and metapsammites: A case study from the Massa Unit (Alpi Apuane, Italy). *Journal of Metamorphic Geology*.
- Pouchou, J.L. & Pichoir, F. 1985. “PAP” phi-rho-Z procedure for improved quantitative microanalysis. In: Microbeam Analysis (ed. J.T. Armstrong), pp. 104– 106. San Francisco Press, San Francisco, CA.
- Pourteau, A., Bousquet, R., Vidal, O., Plunder, A., Duesterhoeft, E., Candan, O., & Oberhänsli, R. (2014). Multistage growth of Fe–Mg–carpholite and Fe–Mg–chloritoid, from field evidence to thermodynamic modelling. *Contributions to Mineralogy and Petrology*, *168*, 1-25.
- Reed, S. J. B. (2005). *Electron microprobe analysis and scanning electron microscopy in geology*. Cambridge university press.
- Ring, U., Glodny, J., Scharf, A., & Hansman, R. (2023). Some like it cold: The ‘conundrum of Samail’ revisited. *Tectonics*, e2022TC007531.
- Seidel, E., Okrusch, M., & Schubert, W. (1975). Chloritoid-bearing metapelites associated with glaucophane rocks in western Crete, Greece. *Contributions to Mineralogy and Petrology*, *49*(2), 105-115.

Theye, T., Seidel, E., & Vidal, O. (1992). Carpholite, sudoite, and chloritoid in low-grade high-pressure metapelites from Crete and the Peloponnese, Greece. *European Journal of Mineralogy*, 4(3), 487-507.

Vidal, O., Theye, T., & Chopin, C. (1994). Experimental study of chloritoid stability at high pressure and various f_{O_2} conditions. *Contributions to Mineralogy and Petrology*, 118(3), 256-270.

Warren, C. J., & Waters, D. J. (2006). Oxidized eclogites and garnet-blueschists from Oman: P–T path modelling in the NCFMASHO system. *Journal of Metamorphic Geology*, 24(9), 783-802.

Whitney, D. L., & Evans, B. W. (2010). Abbreviations for names of rock-forming minerals. *American mineralogist*, 95(1), 185–187.

Yamato, P., Agard, P., Goffé, B., De Andrade, V., Vidal, O., & Jolivet, L. (2007). New, high-precision P–T estimates for Oman blueschists: implications for obduction, nappe stacking and exhumation processes. *Journal of Metamorphic Geology*, 25(6), 657-682.